



# From Single Storms to Global Waves: A Global 2.5 km ICON Simulation of Weather and Climate

Andreas F. Prein<sup>1</sup>, Praveen Pothapakula<sup>1</sup>, Christian Zeman<sup>1</sup>, Morgane Lalonde<sup>1</sup>, and Marius Rixen<sup>1</sup>

<sup>1</sup>Institute for Atmospheric and Climate Science, ETH Zürich, 8092 Zurich, Switzerland

**Correspondence:** Andreas F. Prein (aprein@ethz.ch)

1 **Abstract.** Global kilometer-scale (km-scale) weather and climate models offer new opportunities to unify numerical weather  
2 prediction (NWP) and climate modeling by explicitly simulating convection and mesoscale circulations globally within a single  
3 modeling framework. We present results from the first multi-year (April 2020–March 2024) global atmosphere-land simulation  
4 using the GPU-refactored ICON model at a 2.5 km horizontal grid spacing and 120 vertical levels. The simulation uses NWP  
5 physics and observed sea-surface temperatures. We assess its performance against satellite, reanalysis, and in-situ observations  
6 using standard statistics and the MOAAP feature-tracking framework to evaluate a wide spectrum of atmospheric phenomena.  
7 ICON reproduces global temperature and precipitation patterns, including a realistic single Intertropical Convergence Zone  
8 and physically consistent diurnal precipitation cycles. However, ICON exhibits continental warm and dry biases during the  
9 warm season, linked to an overestimation of incoming solar radiation and excessive surface sensible heat fluxes. The model  
10 realistically captures the intensity and frequency of hourly precipitation and near-surface winds, as well as the structure and  
11 occurrence of tropical cyclones. Mesoscale convective systems (MCSs) exhibit realistic spatial initiation patterns, but their  
12 frequency is underestimated over oceans and overestimated over tropical land. Long-lived MCSs are too infrequent and small,  
13 while excess rainfall from shallow and mid-level clouds suggests overactive warm-cloud microphysics. These biases likely  
14 stem in part from an underrepresentation of convectively coupled equatorial waves. Our results demonstrate the feasibility and  
15 scientific value of multi-year global convection-permitting simulations for exploring the weather–climate system and local-  
16 scale extreme events, while identifying key directions for future model development.

## 17 1 Introduction

18 The consequences of anthropogenic climate change are increasingly visible through record-breaking extreme events and their  
19 associated impacts (e.g., Donat et al., 2016; IPCC, 2023; Seneviratne et al., 2021; Perkins-Kirkpatrick and Lewis, 2020). Reli-  
20 able, local-scale climate information to support adaptation and mitigation efforts is urgently needed, as many extremes and their  
21 impacts occur at spatial scales that are poorly represented in state-of-the-art global climate models (Giorgi and Gutowski Jr,  
22 2015; IPCC, 2023). Kilometer-scale (km-scale) weather and climate models, with horizontal grid spacings of a few kilome-  
23 ters, have emerged as promising tools to bridge this gap by explicitly resolving deep convection, orographic flows, and other  
24 mesoscale phenomena (Prein et al., 2015; Kendon et al., 2017; Lucas-Picher et al., 2021). However, the computational cost of  
25 km-scale modeling has historically restricted its use to limited-area domains over relatively small regions. Recent advances in



26 model development, numerical efficiency, and high-performance computing now allow km-scale simulations to be conducted  
27 globally (Stevens et al., 2019; Schär et al., 2020; World Climate Research Programme, 2022), opening unprecedented op-  
28 portunities to study mesoscale processes and their interactions with synoptic and planetary-scale circulations in a physically  
29 consistent framework.

30 Regional km-scale climate modeling has rapidly evolved over the past decade and has now reached a mature stage of  
31 scientific and technical development (Prein et al., 2015; Ban et al., 2014; Kendon et al., 2021). A central research focus has  
32 been to identify the added value of convection-permitting simulations compared to coarser, convection-parameterized models.  
33 Numerous studies have demonstrated that the intermittency, intensity, frequency, and phase of precipitation are substantially  
34 improved when deep convection is explicitly resolved (e.g., Prein et al., 2013; Ban et al., 2014; Kendon et al., 2017). In  
35 particular, sub-daily precipitation extremes are much better captured (e.g., Ban et al., 2014; Prein et al., 2015, 2017; Ban  
36 et al., 2021; Pichelli et al., 2021) and the diurnal cycle of convective precipitation is more realistically represented (e.g., Ban  
37 et al., 2014; Prein et al., 2013). Furthermore, the spatial organization of convection, including mesoscale convective systems  
38 and tropical cyclones, is substantially improved in km-scale models (e.g., Gentry and Lackmann, 2010; Clark et al., 2016;  
39 Prein et al., 2020, 2021, 2022; Gutmann et al., 2018). Consistent with the explicit treatment of deep convection, km-scale  
40 simulations also produce convective wind gusts and straight-line winds that are absent in models with parameterized convection  
41 (Prein, 2023; Brown et al., 2024). Improved representation of topography enhances the simulation of orographic precipitation,  
42 mountain snow accumulation, and valley wind systems (Liu et al., 2017; Ikeda et al., 2021; Schmidli et al., 2018). Additionally,  
43 km-scale grids allow for a more faithful representation of land–atmosphere coupling, and lateral groundwater fluxes can be  
44 represented explicitly, which can feed back on soil moisture and precipitation characteristics (Hohenegger et al., 2009; Barlage  
45 et al., 2021). At km-scale resolution, urban areas can be better represented, enabling more realistic simulations of urban heat  
46 islands and their influence on local convection and precipitation (Argüeso et al., 2016; Langendijk et al., 2021). However,  
47 dedicated land surface model development efforts are needed to include processes that are typically missing (e.g., shallow  
48 groundwater flow, urban parameterizations).

49 Due to the development of global non-hydrostatic models and advances in computer technology, km-scale global simulations  
50 have become feasible over the last few years. The DYAMOND (DYnamics of the Atmospheric general circulation Modeled On  
51 Non-hydrostatic Domains) intercomparison experiments marked a major step toward global, multi-model, km-scale modeling  
52 by enabling the first coordinated simulations of the atmosphere at grid spacings of 3 km–5 km (Stevens et al., 2019; Takasuka  
53 et al., 2024). These experiments revealed substantial inter-model differences in the ability to simulate mesoscale convective  
54 systems (MCSs) (Feng et al., 2025) and tropical cyclones (Judt et al., 2021). Some modeling systems demonstrated notable  
55 progress following dedicated model development efforts. For instance, the U.S. Department of Energy’s SCREAM (Simple  
56 Cloud-Resolving E3SM Atmosphere Model) initially underestimated convective organization during the first DYAMOND  
57 phase but demonstrated marked improvements in MCS and tropical-cyclone structure in DYAMOND-Winter after major revi-  
58 sions to microphysics and numerics (Taylor et al., 2023; Donahue et al., 2024; Feng et al., 2025). Beyond convective systems,  
59 global km-scale simulations exhibit more realistic representations of equatorial waves and tropical variability compared to  
60 coarser-resolution models (Weber and Mass, 2019; Judt and Rios-Berrios, 2021). Ongoing developments extend these atmo-



61 spheric configurations toward fully coupled Earth system models that include interactive ocean, sea ice, and biogeochemical  
62 components (Segura et al., 2025b).

63 Here, we present an overview of the performance of a global 2.5 km horizontal grid-spacing simulation spanning four con-  
64 secutive years, providing a novel comprehensive assessment of Earth’s hydroclimate and associated extremes at convection-  
65 permitting scales. This simulation represents a major step toward bridging the traditional gap between numerical weather  
66 prediction and climate modeling (Randall and Emanuel, 2024) by explicitly resolving convective processes and mesoscale  
67 storm systems within a global, multi-year integration. We employ a graphics processing unit (GPU)–refactored version of the  
68 ICON (Icosahedral Nonhydrostatic) model (Zängl et al., 2015; Dipankar et al., 2025) using the physical parameterizations from  
69 its operational Numerical Weather Prediction configuration. Such global storm-resolving simulations enable a unified frame-  
70 work for studying the dynamics and statistics of the joined weather–climate system, including tropical cyclones, mesoscale  
71 convective systems, and equatorial waves, and for examining their role in shaping large-scale hydroclimatic variability and  
72 extremes. The primary objectives of this study are threefold: (i) to document the experimental design and technical aspects  
73 of the four-year simulation, (ii) to evaluate its skill in reproducing climate mean states and key mesoscale phenomena and  
74 their contribution to global hydroclimate statistics, and (iii) to identify systematic model deficiencies that can inform future  
75 model development. The resulting dataset, which will be openly released through the DYAMOND-III intercomparison initiative  
76 (Takasuka et al., 2024), provides a novel resource for investigating the physical processes governing the Earth’s hydroclimate  
77 in a high-resolution, fully global context.

## 78 **2 Data and Methods**

### 79 **2.1 Modeling**

80 With recent advances in exascale high-performance computing (HPC) architectures, the computational throughput of various  
81 weather and climate models has substantially improved over the last decade. Especially energy-efficient heterogeneous archi-  
82 tectures, leveraging GPU accelerators, have been developed and can make climate model integrations very efficient (Schär  
83 et al., 2020). However, substantial investments in enabling km-scale weather and climate model codes are needed to port and  
84 efficiently run them on new HPC systems (Donahue et al., 2024; Dipankar et al., 2025). Rapidly emerging technologies in hy-  
85 brid architecture require agile climate model codes that are architecture-agnostic. The EXCLAIM (EXtreme scale Computing  
86 and data platform for cLoud-resolving weAther and cLIimate Modeling) project at ETH Zürich addresses this issue by refac-  
87 toring the ICON code with Domain Specific Language (DSL) with a Python front-end using GridTools for Python — GT4Py  
88 (GT4Py) while enabling backend flexibility across architectures (Paredes et al., 2023; Dipankar et al., 2025).

89 We use the blue line version of the ICON Model (Zängl et al., 2015; Dipankar et al., 2025), developed within the EXCLAIM  
90 project, which features a complete refactoring of the numerical core into GT4Py. Two global experiments were conducted  
91 on the Swiss National Computing Center’s new HPC infrastructure called ALPS. A ten-year (2006–2016) spin-up simulation  
92 was first performed at a 10 km horizontal grid spacing. A 2.5 km grid spacing simulation following the DYAMOND protocol  
93 ((Takasuka et al., 2024)) is conducted for a span of 4 years (January 20, 2020 to April 1, 2024), with its soil state taken from the



94 10 km course grid simulation integrated for 10 years. The 2.5 km simulation uses 240 GH200 GPU nodes (total of 960 GPUs),  
95 achieving a throughput of 0.25 simulated years per day.

96 The 2.5 km simulation uses lower boundary conditions from daily updated sea surface temperatures and the sea-ice fraction  
97 from the ESA Climate Change Initiative (ESA-CCI) product at a horizontal grid spacing of  $1/20^\circ$  (Merchant et al., 2019).  
98 Furthermore, the setup includes 120 vertical levels extending upto 85 km with a terrain-following hybrid setup and the smooth  
99 level vertical (SLEVE) coordinate (Schär et al., 2002). The single-moment cloud Seifert (2008) bulk microphysics scheme is  
100 used to simulate cloud water, ice, snow, graupel, and rain. The second-order turbulent kinetic energy-based surface transfer and  
101 planetary boundary layer parameterization is used for turbulence representation (Raschendorfer et al., 2003). Land processes  
102 are simulated using the TERRA Multi Layer (TERRA-ML) model (Schrodin and Heise, 2001; Grasselt et al., 2008; Schulz  
103 and Vogel, 2020), which employs eight soil layers and is responsible for the exchange of heat, moisture, and momentum. The  
104 TERRA-ML model employs a tile approach to account for accurate cell-averaged surface fluxes, accounting for deviations  
105 in sub-grid-scale surface characteristics. The shallow and deep convection schemes are turned off in the 2.5 km simulation,  
106 allowing an explicit treatment of convection. Additionally, subgrid-scale orographic drag and non-orographic gravity wave  
107 drag schemes are disabled. We used a numerical time step of 20 seconds, updated cloud cover and the microphysics schemes  
108 every time step, and applied the radiation scheme every 6 minutes. The external parameters required by ICON, namely the  
109 topographic height of the Earth's surface, surface roughness, vegetation cover, and land/sea/lake distribution were prepared  
110 using the External Parameters for Numerical Weather Prediction and Climate Application software tool (Asensio et al., 2020).  
111 Finally, we use the global Max-Planck-Institute Aerosol Climatology version 2 (MAC-v2) dataset with  $1^\circ$  grid spacing at a  
112 monthly temporal frequency (Kinne, 2019).

113 The 2.5 km model configuration is close to the ICON-CLM (Climate Limited-area Modelling) community setup and benefits  
114 from vast experience of the community's participation in CORDEX (COordinated Regional Climate Downscaling EXperiment)  
115 activities (Giorgi et al., 2009) across multiple CORDEX regional domains. We did not perform any additional model tuning  
116 for this simulation. We saved output variables following the DYAMOND III protocol (Takasuka et al., 2024).

## 117 **2.2 Observational Datasets**

118 We utilize a range of observational datasets in conjunction with reanalysis to assess the performance of our simulation.

### 119 **2.2.1 ERA5**

120 The ERA5 reanalysis is the fifth-generation global atmospheric reanalysis produced by the European Centre for Medium-Range  
121 Weather Forecasts (ECMWF). It provides hourly estimates of a large number of atmospheric, land-surface, and ocean-wave  
122 variables at a horizontal resolution of about 31 km, spanning from 1940 to the present. ERA5 represents a major improvement  
123 over its predecessor ERA-Interim, particularly in terms of spatial and temporal resolution, as well as uncertainty estimates  
124 (Hersbach et al., 2020). We use ERA5 data to evaluate 2 m above surface temperature.



## 125 **2.2.2 Brightness Temperature**

126 We use two brightness temperature observational products in this study. The NCEP/CPC Level-3 merged infrared brightness  
127 temperatures dataset (Janowiak et al., 2017) provides high-resolution data for deep convective cloud identification and tropical  
128 wave tracking. The NOAA outgoing longwave radiation (OLR) dataset has a much lower resolution (Liebmann and Smith,  
129 1996). It enables the continuous detection of equatorial waves over the simulation period, including slow-evolving waves such  
130 as the Madden-Julian Oscillation.

131 The NCEP/CPC dataset provides gridded equivalent blackbody temperature fields from merged geostationary infrared satel-  
132 lites (Janowiak et al., 2017). It covers latitudes from 60° S to 60° N, with a 4 km horizontal grid and data every 30 minutes. The  
133 product merges observations from multiple geostationary platforms (e.g., METEOSAT, GMS/MTSAT/Himawari, GOES) over  
134 their operational periods. We use full-hour data to track MCSs, non-MCS precipitating cold clouds, and equatorial waves, and  
135 use 30-minute observations to fill gaps in full-hour records.

136 The NOAA OLR dataset provides twice-daily estimates of top-of-atmosphere infrared emission from polar-orbiting satellites  
137 at 2.5° horizontal resolution (Liebmann and Smith, 1996). The dataset extends from 1974 to the present, covering 60° S–60° N,  
138 and offers a consistent long-term record of tropical convective variability. In this study, OLR serves as a large-scale diagnostic  
139 for equatorial wave activity.

## 140 **2.2.3 GPM-IMERGv7 Precipitation**

141 The Integrated Multi-satellite Retrievals for GPM (IMERG) dataset is part of the NASA/JAXA Global Precipitation Mea-  
142 surement mission. It combines observations from a constellation of passive microwave and infrared sensors with gauge data  
143 to provide global precipitation estimates. We use IMERG Final Run version 7, which offers high spatio-temporal resolution  
144 (0.1°, 30-minute) precipitation fields from the year 2000 to the present (Huffman et al., 2020).

## 145 **2.2.4 HadISD Station Observations**

146 The HadISD (Hadley-Centre Integrated Surface Database) is a global sub-daily station dataset based on the NOAA Integrated  
147 Surface Database (ISD), providing quality-controlled observations of key climatological variables such as temperature, dew  
148 point, sea-level pressure, wind speed and direction, and cloud data at individual stations (Dunn et al., 2016; Dunn, 2024). The  
149 dataset currently spans from 1931 to the present and has undergone extensive automated quality control to detect and remove  
150 erroneous values. However, it is not homogenised, and its station density varies over time. We use hourly precipitation and  
151 10 m above surface wind speed records from HadISD v3.4.1 for model validation. Only stations with more than 50 % valid  
152 data coverage during the evaluation period are considered. The location/density of the included station network is shown in the  
153 relevant sections. Station data is compared to data from the nearest ICON grid cell on the native model grid.



## 154 **2.2.5 Surface fluxes: Incoming shortwave and longwave radiation, and latent and sensible heat**

155 We utilize data from 430 flux towers in our model evaluation, sourced from two datasets: FLUXNET (Pastorello et al., 2020)  
156 and AmeriFlux (Chu et al., 2023). These towers provide 30-minute measurements of shortwave and longwave radiation, as well  
157 as surface latent and sensible heat fluxes. Data from these towers is available from 1991 to 2024, with an average record length  
158 of approximately 7 years. The sites are distributed across 43 countries, with denser coverage in North America, Europe, eastern  
159 Asia, and Australia, and sparser representation in Africa and western Asia. It is important to note that inter-annual variability  
160 in surface fluxes contributes to differences between simulations and observations. For reference, across the 430 observational  
161 stations the inter-annual variability, quantified as the standard deviation of annual means, has median values of  $5.2 \text{ W m}^{-2}$  for  
162 SWin,  $3.5 \text{ W m}^{-2}$  for LWin,  $6.7 \text{ W m}^{-2}$  for LE, and  $5.4 \text{ W m}^{-2}$  for H, with interquartile ranges of 3.7–6.8, 2.4–4.6, 4.0–10.5,  
163 and 3.4–8.7  $\text{W m}^{-2}$ , respectively.

164 Additionally, we use gridded surface-downwelling shortwave radiation data from the EWEMBI (Earth2Observe, WFDEI  
165 and ERA-M-B-Ias-corrected) meteorological dataset (Ian, 2016; Lange, 2018) during the period 2012–2016. EWEMBI pro-  
166 vides globally gridded data at  $0.5^\circ$  spatial and daily temporal resolution (calculated as 24-hour averages of hourly fields derived  
167 from 3-hourly fluxes). It combines Earth2Observe data (Schellekens et al., 2017), which uses WFDEI (Weedon et al., 2014)  
168 over land and ERA-Interim over the ocean (Dee et al., 2011), with radiation fields bias-corrected using Surface Radiation  
169 Budget (SRB) observations data released by The GEWEX SRB Project at NASA Langley Research Center (LaRC) (Tren-  
170 berth, 2011) through daily-scale quantile mapping. Although the EWEMBI period (2012–2016) differs from the simulation  
171 period, we include it in the evaluation because interannual variability in surface shortwave radiation is small. The inter-annual  
172 standard deviation of the global mean surface-downwelling shortwave radiation is  $0.3 \text{ W m}^2$ , and the distribution of grid-cell  
173 inter-annual variability shows a mean of  $4.3 \text{ W m}^2$  (IQR:  $2.4 \text{ W m}^2$ – $5.0 \text{ W m}^2$ ). Differences exceeding these ranges can there-  
174 fore be interpreted as significant rather than reflecting natural year-to-year variability.

## 175 **2.2.6 IBTrACS Tropical Cyclone Characteristics**

176 The IBTrACS (International Best Track Archive for Climate Stewardship) dataset is a comprehensive global compilation of  
177 tropical cyclone “best track” data, aggregated from multiple official agencies across all ocean basins. It provides information  
178 on storm position, intensity (e.g. maximum sustained winds and/or minimum central pressure), and other parameters, typically  
179 at 3-hour or 6-hour intervals, spanning from the mid-19th century to the present (Knapp et al., 2010; Gahtan et al., 2024). The  
180 project also records the original reports from contributing agencies and summary statistics (such as the mean track and range  
181 across agencies) to facilitate intercomparison. We use U.S. records from IBTrACS v4.01 (specifically the variables ‘usa\_wind’  
182 and ‘usa\_pres’) since they are most up-to-date and contain information on recent tropical cyclone activity globally. Recorded  
183 speed correspond to maximum sustained wind averaged over 1 minute at 10 m above surface.



## 184 2.3 Methods

### 185 2.3.1 Atmospheric feature tracking with the MOAAP algorithm

186 The Multi-Object Analysis of Atmospheric Phenomenon (MOAAP; Prein et al. (2023b)) algorithm is an automated, object-  
187 based framework that identifies and tracks a wide range of atmospheric systems using a minimal set of commonly available  
188 reanalysis and model variables. MOAAP combines 12 key atmospheric variables from observations (here ERA5 reanalysis,  
189 GPM IMERG precipitation, and GPM\_MERGIR cloud-top brightness temperature) and the ICON model to consistently detect  
190 and track features such as tropical and extratropical cyclones, cut-off lows, anticyclones, frontal zones, jet streams, moisture  
191 streams, mesoscale convective systems (MCSs), and equatorial waves.

192 Feature detection is based on a connected-component approach applied in space and time. The algorithm first thresholds  
193 relevant variables to form binary masks of regions exceeding physically motivated intensity criteria. It then labels contigu-  
194 ous three-dimensional (latitude–longitude–time) structures using the `ndimage.label` function from SciPy (Virtanen et al.,  
195 2020). In a second step, features are segmented based on the existence of multiple minima/maxima within an object using  
196 the `skimage.segmentation` and `skimage.feature` functionalities and applying watershed segmentation. Phenom-  
197 ena are then identified according to temporal persistence rules and phenomenon-specific geometric, temporal, and intensity  
198 thresholds. Each identified object is assigned physical characteristics such as area, duration, maximum intensity, and center of  
199 mass, which enable subsequent statistical and climatological analyses. MOAAP provides a unified, reproducible framework  
200 for quantifying and intercomparing the contributions of different atmospheric phenomena to mean and extreme precipitation  
201 across spatial and temporal scales.

202 The MCS analysis in section 3.7 is performed on a global  $0.1^\circ$  regular grid that corresponds to the GPM-IMERG grid.  
203 GPM-MERGIR and ICON data are conservatively regridded to this grid. Additionally, the hourly heavy precipitation analysis  
204 in section 3.9 is performed on a standard  $0.25^\circ$  mesh that corresponds to the ERA5 grid. The only phenomenon not included in  
205 MOAAP that we were unable to identify is atmospheric rivers, as ICON lacks an IVT diagnostic. More details about MOAAP  
206 can be found in (Prein et al., 2023b, 2024; Feng et al., 2025).

### 207 2.3.2 Deriving central pressure, maximum wind, and pressure–wind pairs

208 We use tropical cyclones (TCs) identified by MOAAP to calculate TC intensity centered on the TC sea level pressure (SLP)  
209 minima at each time step (hour). Distances and azimuths are computed using great-circle geometry and land-sea ocean points  
210 are defined via a land-sea mask with a 30 km coastal buffer. The maximum sustained wind  $V_{\max}$  is the peak 10-m wind speed  
211 from hourly instantaneous model output within the inner-core disk given by the Reference Disk Radius (RDR), defined as

$$212 \text{RDR} = \min(\text{RMW}, r_{\partial p}),$$

213 where  $\text{RMW} = \arg \max_r \overline{|u_t|}(r)$  is the radius of maximum mean tangential wind and  $r_{\partial p} = \arg \max_r |\partial \bar{p} / \partial r|$  is the radius of  
214 strongest radial SLP gradient (Knaff and Zehr, 2007; Schenkel and Hart, 2012).



## 215 **3 Results**

216 We start this section with a climatological analysis of near-surface temperature, surface fluxes, and precipitation, followed  
217 by assessing higher-order statistics of hourly precipitation and surface wind speed, and ending with evaluating the fidelity of  
218 simulating atmospheric storms such as TCs, MCSs, and extreme precipitation-producing systems.

### 219 **3.1 2 m above surface temperature (T2M)**

220 The global average pattern of T2M is well simulated with a Spearman pattern correlation coefficient of 0.998 and a root mean  
221 squared error of 1.48 °C for land grid points (Fig. 1). As expected, ocean regions exhibit particularly small differences due to  
222 the pre-described sea surface temperature. Striking are cold differences in ICON during polar winters that might be related to  
223 the representation of sea ice and snow in addition to differences stemming from uncertainties in ERA5 T2M in these regions  
224 (Fig. 1d,f). Larger differences also occur during boreal winters over land areas with up to 3 °C negative differences in eastern  
225 Canada and large positive differences in Siberia and Alaska.

226 During boreal summers, temperatures exceeding 3 °C warm differences emerge in continental regions such as the central  
227 U.S. and Eurasia (Fig. 1f). Part of these differences is likely related to a misrepresentation of land-atmosphere interactions,  
228 such as the lack of lateral groundwater flow and the corresponding reduced evapotranspiration in land-atmosphere coupling  
229 hot-spots such as the central U.S., which can cool down these regions by several degrees Celsius (Barlage et al., 2021).

230 It is important to note that the differences shown here and in the following sections are partly related to the short simulation  
231 period of four years. Climate internal variability can cause large differences at local scales (Deser et al., 2012) even though  
232 observed sea surface temperatures are used.

### 233 **3.2 Surface fluxes: Incoming shortwave and longwave radiation, and latent and sensible heat**

234 Fig. 2 shows the daily mean surface incoming shortwave radiation (SWin) for (a) ICON, (b) the EWEMBI observational  
235 dataset, and (c) their difference. Overall, SWin is underestimated over oceans, especially along the Intertropical Convergence  
236 Zone, and overestimated over land, particularly in mountainous regions. This overestimation over land is also evident when  
237 comparing the simulation to flux tower observations (Fig. 2d,e). The median difference in land mean SWin is approximately  
238 6.8 W m<sup>-2</sup>, with a median difference of around 25 W m<sup>-2</sup> at noon, which is similar to the approximately 7.8 W m<sup>-2</sup> mean bias  
239 found in CMIP6 models (He et al., 2023). The representation of shallow clouds is frequently a main contributor to these biases  
240 in models with convection parameterizations (e.g., Ahlgrimm and Forbes, 2012) and km-scale models (e.g., Sakradzija et al.,  
241 2020; Lucas-Picher et al., 2024).

242 Fig. 2d and e show the spatial distribution of station median total and noon differences in longwave downward radiation  
243 (LWin), latent heat flux (LE), and sensible heat flux (H). LWin is slightly underestimated. LE shows a median difference  
244 close to zero across stations, with regionally over- and underestimations of more than 10 W m<sup>-2</sup> that cancel each other on  
245 average. This suggests that some land surface processes, such as vegetation transpiration or soil evaporation, may not be



246 adequately captured by the model. In contrast, H is more consistently overestimated, particularly during noon, agreeing with  
247 the overestimation in SWin.

248 The spatial pattern of station-based mean noon differences in LE and H during JJA shows a pronounced underestimation of  
249 LE and an overestimation of H at most stations in ICON (Fig. 2f,h) in agreement with the T2M differences shown in Fig. 1.  
250 We attribute parts of the systematic dry-summer biases to the absence of a lateral subsurface water-flux scheme in TERRA.  
251 Previous studies have shown that the lack of such lateral groundwater redistribution can lead to substantial surface flux and  
252 temperature biases at km-scale grid spacing (Barlage et al., 2021; Soares et al., 2024). In contrast, winter biases appear to be  
253 more site-specific. The spatial consistency and agreement of the surface flux differences with biases in other variables indicate  
254 that these results are robust.

### 255 3.3 Precipitation (PR)

256 Annual and seasonal differences between ICON and GPM-IMERG are shown in Fig. 3. The Pearson pattern correlation of  
257 annual average precipitation is 0.91 (0.87 over land cells) and the corresponding relative RMSE is 41 %. Most noticeable are  
258 wet differences over most tropical ocean regions except for the west Maritime Continent (Fig. 3c). This is consistent with the  
259 negative SWin differences shown in Fig. 2c. Land precipitation is relatively well simulated with dry differences in continental  
260 regions during boreal summer (Fig. 3g) colocated with warm differences in Fig. 1f and higher SWin, lower LE, and higher H.

261 Zonal average precipitation agrees very well between GPM-IMERG and ICON, partly because of error cancellation effects  
262 (Fig. 3d). The differences are typically smaller than the inter-annual variability (shading in Fig. 3d) except for high-latitudes  
263 where IMERG is known to underestimate precipitation accumulations due to issues in remote sensing solid precipitation (Song  
264 et al., 2021) complicating a reliable evaluation. The location of the wet regions in the tropics (defined as the 80th percentile of  
265 tropical average precipitation; Fig. 3h) is remarkably well captured with a single tropical rainband.

266 This is a big achievement since simulating a realistic rainband is challenging, even at a km grid spacing as Segura et al.  
267 (2025b) found a double ITCZ in the Indo-Pacific using km-scale ICON simulations with model physics different from ours.  
268 They found a lack a surface fluxes (caused by too little surface winds) in this region, which they resolved by increasing the  
269 minimum surface wind speed in the lowest model level from  $1 \text{ m s}^{-1}$  to  $4 \text{ m s}^{-1}$  (Segura et al., 2025a). Our model settings,  
270 which are similar to ICON's NWP setup, do not feature this issue. While it is unclear what exactly causes the differences  
271 in model performance between the ICON setups, a key difference lies in the turbulence parameterizations and surface layer  
272 schemes.

273 Comparing peak hourly precipitation over the four-year evaluation period between GPM-IMERG and ICON shows that our  
274 simulation yields substantially larger values, particularly in the tropics and subtropics (Fig. 4a,b). This is predominantly caused  
275 by too low heavy hourly precipitation in GPM-IMERG since comparisons with hourly precipitation gauge observations from  
276 the HadISD dataset show that ICON reliably reproduces observed intense precipitation rates across various climate regions.  
277 At the same time, GPM-IMERG fails to capture intense rates, particularly at lower latitudes (Fig. 4c–f), which is in agreement  
278 with previous research (Dominguez et al., 2024; Yu et al., 2025). However, a proper evaluation of hourly precipitation using  
279 station data is not possible in many parts of the globe due to insufficient data coverage and a lack of data sharing (e.g., Prein and



280 Gobiet, 2017). Our presented analysis is primarily based on data from the U.S. and Europe (see Fig. S1). Results for additional  
281 climate regions, often based on only a few stations, are shown in Fig. S2.

282 Using the same station network, we assess the June-July-August (JJA) season-average precipitation diurnal cycle (Fig. 5; we  
283 use  $0.1 \text{ mm h}^{-1}$  as the threshold for precipitation intensity and frequency statistics). The performance of ICON is regionally  
284 dependent and shows good agreement for capturing precipitation amount, frequency, and intensity in the North Central Amer-  
285 ica (NCA) region that is heavily influenced by the North American Monsoon (Fig. 5g-i). In Eastern North America (ENA),  
286 precipitation frequency is well captured compared to station data. Still, precipitation intensity is overestimated, resulting in an  
287 overly amplified evening and nocturnal peak in precipitation amplitudes (Fig. 5a-c). Western Central Europe (WCE) shows a  
288 too early peak in precipitation that decays too quickly. The precipitation amount is also low-biased due to the too infrequent  
289 simulation of precipitation. Generally, ICON shows greater fidelity in capturing the diurnal cycle of convective precipitation in  
290 southern regions (ENA and NCA) than GPM-IMERG.

291 From Fig. 5, we see that the peak timing of convective precipitation amount is relatively well captured by GPM-IMERG,  
292 consistent with previous findings (e.g., Dominguez et al., 2024). This allows us to evaluate ICON on a near-global scale  
293 (Fig. 6). We perform this analysis during seasons dominated by convective precipitation, namely JJA at  $>30^\circ\text{N}$ , December-  
294 January-February (DJF) at  $<30^\circ\text{S}$ , and annually in the tropics. GPM-IMERG and ICON feature afternoon precipitation peaks  
295 over land. In contrast, tropical ocean regions feature predominantly nighttime and early-morning peaks. Some land regions  
296 also feature nocturnal precipitation peaks, particularly in the lee of mountain ranges (e.g., the central U.S., the La Plata basin,  
297 eastern China, and the Sahel and Western Africa), which are related to nocturnal mesoscale convective system activity. ICON  
298 can capture these nocturnal peaks reasonably well, but the spatial extent of nocturnal regions is often too small, particularly in  
299 the Amazon Basin and the central U.S. The relative amplitude of the convective precipitation diurnal cycle (diurnal amplitude  
300 divided by mean precipitation) is also relatively similar, with a tendency for larger values in ICON compared to GPM-IMERG.

### 301 **3.4 Near surface winds (UV10)**

302 Tropical cyclones cause the most intense UV10 extremes during the evaluation period (Fig. 7a). Storm tracks of extratropical  
303 cyclones are also clearly visible in both hemispheres. Over land, mountain regions and plateaus such as the Tibetan Plateau and  
304 the Andes stand out, as do mid-latitude plains that feature straight-line windstorms (e.g., the central U.S., the La Plata Basin,  
305 and the Sahel). Also, the coastal regions of Greenland and Antarctica feature peak wind speeds exceeding  $40 \text{ m s}^{-1}$ .

306 Evaluations against UV10 HadISD station observations show overall good agreement with a tendency of heavy wind speeds  
307 ( $>20 \text{ m s}^{-1}$ ) to be underestimated in ICON (Fig. 7b). However, regional differences are observed, with lower differences at  
308 high wind speeds, mostly in Mid-Latitude regions such as CNA and WCE (Fig. 7c,d). The region with the most pronounced  
309 underestimation of UV10 extremes is Eastern North America (Fig. S4), which might be partly related to a low difference in  
310 tropical cyclone frequency as we will see in section 3.5. Intense winds are well simulated in most tropical and high latitude  
311 areas such as East Asia (EAS) and Northern Australia (NAU) (Fig. 7e,f). The station density that is available for comparison in  
312 HadISD is shown in Fig. S3, and statistics for additional IPCC regions are shown in Fig. S5. Also, the temporal autocorrelation



313 of hourly winds is well simulated in ICON, indicating that the structure of wind-producing storms and weather systems is  
314 reasonably well simulated (Fig. S4).

315 The wind speed evaluation should be interpreted with caution, as we compare station data with 2.5 km grid-cell averages.  
316 Additionally, short-term average wind speeds (e.g., 2-minute averages at U.S. stations, 10-minute averages at many WMO  
317 stations) are compared with hourly instantaneous model winds. Instantaneous model snapshots tend to produce broader, higher-  
318 tailed wind-speed PDFs than temporally averaged station observations, while spatial averaging over 2.5 km grid cells damps  
319 small-scale wind maxima. The combined effect partially compensates for differences.

### 320 3.5 Tropical cyclones

321 Tropical cyclone tracks compare well in frequency and location between ICON and IBTrACS, except for the North Atlantic  
322 Basin, which features a low bias (Fig. 8a,b). Note that the longer tracks in IBTrACS are caused by identifying TCs already as  
323 tropical depressions and following them after the extra-tropical transition. In contrast, MOAAP only identifies the main TC  
324 phase. The inter-annual variability of basin total tropical cyclone frequencies is also well captured in ICON, except for the  
325 Southwest Pacific and South Indian Ocean, where the variability is smaller (Fig. 8b).

326 The TC pressure wind relationship is relatively well captured, but ICON wind speeds are too low (Fig. 8c), consistent with  
327 the UV10 analysis in the previous section. The low difference is also reflected in the probability histogram of tropical cyclone  
328 lifetime peak wind speeds, which drops off too rapidly at high wind speeds (Fig. 8d). The IBTrACS distribution shows a bi-  
329 modal distribution with a minimum around  $40 \text{ m s}^{-1}$  and a primary peak at low wind speeds. The reason for this primary peak  
330 is that the tropical depression and tropical storm phases of TC are included in IBTrACS. In contrast, the MOAAP tracker is  
331 calibrated to only identify storms with tropical storm intensity.

### 332 3.6 Equatorial waves

333 (Fig. 9) shows Hoffmüller diagrams of tropical average brightness temperatures in ICON and GPM-MERGIR, with labels  
334 indicating equatorial waves from MOAAP output for May 2020. While Rossby waves are well simulated in ICON, other  
335 strongly coupled waves to deep convection are underestimated in both frequency and amplitude. Kelvin and inertia-gravity  
336 waves (IGWs) are very infrequent, and Mixed Rossby-Gravity Waves (MRGs) are only regularly observed over Africa.

337 Global kilometer-scale (storm-resolving) models substantially improve the simulation of convectively coupled equatorial  
338 waves by explicitly representing deep convection, leading to more realistic precipitation spectra, wave propagation, and dy-  
339 namical structures compared to models with parameterized convection (??). However, despite these advances, biases remain  
340 in wave–convection coupling strength, phase speed, and intermittency, indicating that the representation of equatorial waves at  
341 km-scale resolution is improved but still model- and configuration-dependent rather than fully resolved (??).

342 (Jung and Knippertz, 2023)

343 Wheeler–Kiladis space–time spectra computed from the four-year evaluation period confirm these results (Fig.,10). We fol-  
344 low the approach of Wheeler and Kiladis (1999) and apply it to outgoing longwave radiation (OLR) from the ICON simulation  
345 and the NOAA-interpolated OLR dataset. Overall, ICON reproduces the observed spectral characteristics of equatorial waves



346 reasonably well. Rossby wave activity shows the closest agreement with observations, while other modes—such as Kelvin  
347 waves, the Madden–Julian Oscillation (MJO) and IGW—are captured but exhibit lower amplitudes than in the NOAA OLR  
348 data.

### 349 **3.7 Mesoscale convective systems (MCSs)**

350 Equatorial waves often organize convection into clusters of MCSs. The latent heating from these MCSs can, in turn, amplify  
351 and maintain the wave, creating a feedback between the large-scale disturbance and the convection (Kiladis et al., 2009). The  
352 general pattern of MCS initiation frequency is well captured in ICON, but initiation is underestimated over tropical oceans and  
353 overestimated over tropical land regions (Fig. 11a–c). The relative underestimation of oceanic MCS frequency is largest in the  
354 northern hemisphere, followed by the southern hemisphere, and tropics (Fig. 11g–i). In the tropics, oceanic MCS frequencies  
355 are well simulated between December and March but have a systematic low bias in the other months of the year (Fig. 11h).

356 Simulated land-based MCSs frequencies are most similar to observations in the northern hemisphere. Frequencies are over-  
357 estimated in the southern hemisphere during summer and in the tropics throughout the year, except in June and July.

358 These frequency biases result in a systematic underestimation of the MCS to total precipitation ratio over almost all ocean  
359 regions, while this ratio is overestimated over Africa (Fig. 11d–f). The reasons for the MCS frequency biases are unclear but  
360 they are likely related to biases in tropical waves, which will be the topic of future research.

361 In addition to frequency statistics, we also performed lifetime analysis of oceanic and land-based MCSs in the tropics,  
362 northern, and southern hemispheres (Fig. 12 and Fig. S6 and S7 respectively). We discuss only the results from the tropics  
363 here, since they are similar in both hemispheres. Observed MCS sizes are similar over tropical oceans and land (Fig. 12a).  
364 Simulated MCSs are generally smaller than observed systems. This bias is larger over the ocean than over land. The simulated  
365 MCS movement speed is systematically higher for most quintiles (Fig. 12b), while the mean precipitation under the MCS cloud  
366 shields is lower (Fig. 12c), particularly for land-based MCSs. Finally, modeled MCS durations are too short (2–4 hours median  
367 difference), with larger differences over land than over ocean (Fig. 12d).

368 To compare the temporal evolution of MCSs, we differentiate between short-lived (4–9 hours) and long-lived (>14 hours)  
369 tropical MCSs, given lifetime-dependent model biases. The growth and decay of MCS cloud shields are well simulated for  
370 oceanic and land-based tropical MCSs (Fig. 12e,f). However, long-lived storms do not grow fast enough and reach a peak size  
371 that is about 20–30 % too small. On the other side, long-lived storms feature more accurate movement speeds while small  
372 storms move about 20 % too fast (Fig. 12g,h).

373 Mean MCS precipitation starts high during the initiation phase of MCSs and steadily decreases during their lifetime (Fig. 12i,j).  
374 This is because most MCSs start from a burst of small-scale convection and develop stratiform precipitation areas as they grow  
375 upscale until the convective areas die off in the decaying phase, resulting in mostly stratiform precipitation (e.g., Mapes et al.,  
376 2006). ICON simulates mean precipitation within  $\pm 20\%$  of observed values during the growth phase with the exception of  
377 land-based long-lived systems that have a high difference of up to 40 %. Simulated mean MCSs precipitation becomes increas-  
378 ingly low-biased over the life cycle of storms ending at low differences of up to -60 % during the decaying phase. This indicates



379 difficulties in simulating MCS stratiform precipitation, which is a common issue in many km-scale models (e.g., Prein et al.,  
380 2023a; Zhang et al., 2024).

381 Finally, the combined differences in mean precipitation rates and MCS size are affecting the differences in MCS precipitation  
382 volume, which is better simulated during the growth phase but becomes increasingly negatively biased over their lifetime,  
383 especially for short-lived systems (Fig. 12k,l). The dominant driver of this bias is the low mean precipitation difference for  
384 short-lived systems, as well as the low size difference for long-lived storms. We refrain from analyzing differences in the  
385 development of heavy precipitation rates due to the deficiencies in capturing these in GPM-IMERG (see Fig. 4.)

### 386 **3.8 Precipitating cloud characteristics**

387 We found some of the largest model wet biases in tropical ocean ITCZ precipitation (Fig. 3). At the same time, MCSs are  
388 to infrequent in this region. To better understand the source of this bias we also tracked smaller precipitating cloud systems  
389 that have cold cloud tops in addition to MCSs (see section 2.3.1 and Fig. 13a–c). As previous studies have shown, cloud  
390 sizes (i.e., cold cloud top areas) follow a power-law frequency distribution (e.g., Savre and Craig, 2023). Observations show  
391 that cold cloud shields that exceed our MCS threshold ( $>40,000 \text{ km}^2$ ) contribute the most to tropical precipitation with a  
392 maximum contribution from clouds with  $\sim 75,000 \text{ km}^2$  (Fig. 13a). This maximum is shifted towards smaller cloud sizes and  
393 lower volumes in ICON (Fig. 13b) with a low contribution bias for large clouds and an overestimation from small clouds  
394 (Fig. 13c). Not visible in Fig. 13 are the low frequency biases in MCSs and non-MCS precipitating cold clouds (Fig. S10) since  
395 normalized distributions are shown.

396 A key question is: which clouds cause the excess simulated precipitation in the tropics if deep convective clouds are too  
397 infrequent and too small? Fig. 13d–f show that in observations, most tropical precipitation originates beneath cold cloud tops,  
398 while ICON simulations have a too large fraction of rainfall coming from warm clouds. This issue is particularly evident in  
399 tropical land and ocean regions, but is also evident to a lesser extent in the Northern and Southern hemispheres (Fig. S8 and  
400 Fig. S9). Excess precipitation from clouds with warm cloud tops indicates overly active warm cloud processes or too slow  
401 glaciation of tropical clouds in the ICON microphysics scheme.

### 402 **3.9 Drivers of heavy precipitation**

403 The output from the MOAAP algorithm allows us to analyze the interactions among atmospheric phenomena in creating hourly  
404 heavy precipitation events in observations and in the ICON model (Fig. 14). We decided to exclude equatorial waves and fronts  
405 from the analysis in Fig. 14a–f since equatorial waves dominate tropical heavy precipitation statistics due to their large size,  
406 and including them obscures details from smaller-scale phenomena (Fig. S11). We decided to exclude fronts because they are  
407 more frequent in ICON, likely due to its higher model resolution, which allows sharper gradients to be simulated. Results  
408 including fronts and equatorial waves are shown in Fig. S11.

409 ICON can effectively simulate the processes that cause extreme precipitation across different climate regions, though it  
410 has some notable deficiencies. In observations, MCSs are more often the most frequent producers of heavy precipitation in  
411 tropical and subtropical ocean regions (Fig. 14a,b). This agrees with our previous analysis, which showed low-frequency and



412 size differences in simulated MCSs. In contrast, simulated MCSs are more dominant over tropical and subtropical land regions,  
413 where observations highlight non-MCS cold clouds as most important. At the same time, moisture streams (areas of low-level  
414 strong and coherent horizontal moisture transport) are frequently more relevant in ICON than in observations, particularly in  
415 subtropical ocean regions.

416 Fig. 14g–i show frequency statistics that visualize how often a phenomenon was co-located with hourly heavy precipitation  
417 in the Northern European (NEU), Southeast South America (SES), and the Equatorial Pacific Ocean (EPO) region. In the high-  
418 latitude NEU region, observations and ICON agree that surface cyclones and mid-level cyclones are the most frequent drivers  
419 with secondary contributions from jet streams and moisture streams (Fig. 14g). ICON features more heavy precipitation events  
420 from non-MCS clouds than observed and a larger contribution of frontal systems. Cut-off lows are less frequently involved in  
421 simulated heavy precipitation events than in observations.

422 In the SES region, ICON agrees with observations that MCSs and non-MCS clouds are the dominant heavy precipitation-  
423 producing phenomena (Fig. 14h). ICON also captures the importance of moisture streams and jet streams well, while frontal  
424 involvement is much higher than in ERA5.

425 We find a relatively poor agreement in the tropical EPO region (Fig. 14i) where ICON substantially underestimates the  
426 importance of MCSs and all equatorial waves except for Equatorial Rossby waves, in agreement with previously shown re-  
427 sults. However, ICON can capture the importance of non-MCS cold clouds and moisture streams in the production of heavy  
428 precipitation.

#### 429 **4 Summary and Conclusion**

430 We present results from the first multi-year (April 2020–March 2024), global prescribed SST convection-permitting simulation  
431 performed with the GT4Py GPU-refactored ICON model (Dipankar et al., 2025) at a horizontal grid spacing of 2.5 km and  
432 120 vertical levels. This experiment, conducted within the EXCLAIM project, represents a major milestone in bridging the  
433 long-standing divide between numerical weather prediction (NWP) and climate modeling (Randall and Emanuel, 2024), using  
434 a model configuration based on operational forecasting without empirical tuning. By explicitly resolving deep convection,  
435 orographic drag, mesoscale circulations, and local land heterogeneity on a global scale, the model enables the consistent study  
436 of weather and climate processes within a unified physical framework.

437 We conducted a comprehensive evaluation using satellite, reanalysis, and in-situ observations to assess the fidelity of the  
438 simulation of atmospheric phenomena at scales ranging from global to local. The following main points summarizing our  
439 study:

- 440 – The ICON model reproduces observed large-scale patterns of temperature, precipitation, and surface energy fluxes with  
441 high fidelity, showing good agreement with reanalysis, satellite, and in situ observations. Importantly, the model can  
442 realistically simulate the spatial pattern of tropical precipitation with a single ITCZ. However, there is an overestimation  
443 of tropical oceanic clouds (up to -40% in incoming shortwave radiation at the surface) and precipitation (up to 50%)  
444 and cold biases in polar regions (more than -3 °C) during winter. Additionally, warm biases over mid-latitude conti-



445 nents during the warm season are related to too much incoming solar radiation, an underestimation in latent- and an  
446 overestimation of sensible heat fluxes.

447 – Explicitly resolving convection yields a realistic convective diurnal cycle and an excellent representation of the hourly  
448 rainfall probability density distribution, including extremes. Still, some land regions, such as those over southern Africa,  
449 Australia, and parts of the Amazon basin, feature a too early diurnal precipitation peak.

450 – Near-surface winds and tropical cyclone statistics are generally well simulated, but maximum wind speeds are underes-  
451 timated by  $\sim 20\%$ . Tropical cyclone frequencies are well captured, except in the North Atlantic basin, where low biases  
452 are observed, similar to other high-resolution climate model simulations (Roberts et al., 2020).

453 – Spatial initiation patterns of MCSs are realistic, but ICON underestimates oceanic MCS frequencies (especially outside  
454 DJF) and overestimates tropical land MCSs. Simulated systems are smaller, slightly too fast, and too short-lived, resulting  
455 in an underestimation of MCS precipitation over oceans and an overestimation over some tropical land areas. The low  
456 bias in tropical MCS precipitation and the underestimation of MCS size are common among km-scale global models  
457 (Feng et al., 2025). The low-frequency bias in long-lived, large MCSs contributes to the earlier peak timing in the  
458 convective diurnal cycle.

459 – Since both precipitation from MCS and non-MCS cold clouds is underestimated over tropical ocean regions, it is unclear  
460 which clouds are causing the oceanic wet tropical precipitation bias in ICON. The primary cause is excessive simulated  
461 rainfall from shallow and mid-level clouds (e.g., cumulus congestus). The reason for this bias is unclear, but it is likely  
462 related to an overactive warm rain process.

463 – The frequency and amplitude of all equatorial waves except for Rossby waves are underestimated. This is consistent with  
464 the underestimation of MCSs and the overestimation of precipitation from shallow clouds in the tropics since equatorial  
465 waves are frequently coupled to deep convection (Kiladis et al., 2009; Prein et al., 2023b). Km-scale global models tend  
466 to capture equatorial Rossby waves well since their dynamics are controlled by large-scale vorticity gradients rather  
467 than the details of convective heating. In contrast, Kelvin, MRG, inertia–gravity waves, and the MJO require coherent  
468 two-way coupling of deep convection and large-scale dynamics to maintain amplitude and propagation (e.g., Kiladis  
469 et al., 2009; Judt and Rios-Berrios, 2021). Additionally, ocean-atmosphere interactions are important for simulating  
470 connectively coupled equatorial waves, which our forced SST setup does not capture (e.g., DeMott et al., 2015).

471 – An object-based evaluation using the MOAAP feature tracker (Prein et al., 2023b) reveals that ICON realistically cap-  
472 tures the main meteorological drivers of heavy hourly precipitation, including cyclones, MCSs, and moisture streams.  
473 Consistently, we find deficiencies in simulating heavy rainfall from tropical oceanic MCSs and equatorial waves.

474 In summary, the EXCLAIM 2.5 km global ICON simulation provides a unique benchmark for studying global hydrocli-  
475 matic extremes and mesoscale dynamics. It will serve as a contribution to the DYAMOND-III intercomparison initiative (Taka-  
476 suka et al., 2024), allowing for comparison with an ensemble of km-scale global models. The simulation offers novel insight



477 into the interplay between convection, large-scale circulation, and climate variability. Current ICON developments within the  
478 EXCLAIM project aim to optimize the code for faster runtime and to implement ocean-atmosphere coupling at km-scales  
479 (Dipankar et al., 2025).

480 While notable challenges remain in representing tropical variability, mesoscale convective organization, and land-atmosphere  
481 coupling, the demonstrated capability of the model establishes a new foundation for next-generation Earth system modeling  
482 and the transition toward truly unified weather–climate simulations.

483 *Code and data availability.* NOAA Interpolated Outgoing Longwave Radiation (OLR) data were provided by the NOAA Physical Sciences  
484 Laboratory (PSL), Boulder, Colorado, USA, from their website at <https://psl.noaa.gov>.

485 The global 2.5 km ICON simulation was produced within the EXCLAIM project following the DYAMOND-III protocol and will be made  
486 publicly available through the DYAMOND-III intercomparison archive upon completion of the coordinated data release. Until then, access  
487 can be provided by the corresponding author upon reasonable request.

488 All observational and reanalysis datasets used in this study are publicly available, including ERA5 reanalysis (<https://cds.climate.copernicus.eu/datasets/reanalysis-era5-single-levels?tab=overview>), GPM-IMERG precipitation (<https://gpm.nasa.gov/resources/documents/imerg-v07-release-notes>), merged infrared brightness temperatures (<https://gpm.nasa.gov/data/directory/ncep-cpc-level-3-merged-infrared-brightness-temperatures-0>), HadISD station observations (<https://www.metoffice.gov.uk/hadobs/hadisd/>), FLUXNET (<https://fluxnet.org/data/fluxnet2015-dataset/>), AmeriFlux surface flux measurements (<https://ameriflux.lbl.gov/data/how-to-upload-data/>), IBTrACS tropical cyclone data (<https://www.ncei.noaa.gov/products/international-best-track-archive>), and the EWEMBI surface radiation dataset (<https://www.isimip.org/gettingstarted/input-data-bias-adjustment/details/27/>).

495 Code that was used for the analysis and visualization of the presented results can be accessed from Prein (2025) and <https://doi.org/10.5281/zenodo.18007290>.

497 *Author contributions.* AFP designed, conceptualized, performed most of the analyses, and wrote the first draft of the manuscript. PP ran the  
498 ICON simulations and archived the data with support from CZ. ML performed the surface flux analyses and MR performed the Wheeler and  
499 Kiladis analysis. All authors contributed to the writing of the paper.

500 *Competing interests.* We do not have any competing interests.

501 *Acknowledgements.* This work was supported by a grant from the Swiss National Supercomputing Centre (CSCS) under the EXCLAIM  
502 project on Alps. The authors thank the NOAA Physical Sciences Laboratory (PSL), Boulder, Colorado, USA, for providing the Interpolated  
503 Outgoing Longwave Radiation (OLR) dataset, available at <https://psl.noaa.gov>. ERA5 reanalysis data were obtained from the Copernicus  
504 Climate Change Service (C3S) Climate Data Store. The GPM IMERG data were provided by the NASA/Goddard Space Flight Center's  
505 Global Precipitation Measurement and PPS, which develop and compute the GPM IMERG as a contribution to GPM, and archived at



506 the NASA GES DISC. Merged infrared brightness temperature data were provided by NASA and NOAA. We acknowledge the UK Met  
507 Office for HadISD station observations, the FLUXNET and AmeriFlux networks and their contributing site investigators, NOAA/NCEI for  
508 IBTrACS tropical cyclone data, and ISIMIP for providing the EWEMBI surface radiation dataset. We used Grammarly and ChatGPT to  
509 support the writing of this manuscript.



## 510 References

- 511 Earth2Observe, WFDEI and ERA-Interim data Merged and Bias-corrected for ISIMIP (EWEMBI), author=Lange, Stefan, (No Title), 2016.
- 512 Ahlgrimm, M. and Forbes, R.: The impact of low clouds on surface shortwave radiation in the ECMWF model, *Monthly Weather Review*,  
513 140, 3783–3794, 2012.
- 514 Argüeso, D., Di Luca, A., and Evans, J. P.: Precipitation over urban areas in the western Maritime Continent using a convection-permitting  
515 model, *Climate dynamics*, 47, 1143–1159, 2016.
- 516 Asensio, H., Messmer, M., Lüthi, D., and Osterried, K.: External Parameters for Numerical Weather Prediction and Climate Ap-  
517 plication EXTPAR v5\_0, User and Implementation Guide. Available online: [http://www.cosmo-model.org/content/support/soft-](http://www.cosmo-model.org/content/support/software/ethz/EXTPAR_user_and_implementation_manual_202003.pdf)  
518 [ware/ethz/EXTPAR\\_user\\_and\\_implementation\\_manual\\_202003.pdf](http://www.cosmo-model.org/content/support/software/ethz/EXTPAR_user_and_implementation_manual_202003.pdf) (accessed on 16 November 2018), 2020.
- 519 Ban, N., Schmidli, J., and Schär, C.: Evaluation of the convection-resolving regional climate modeling approach in decade-long simulations,  
520 *Journal of Geophysical Research: Atmospheres*, 119, 7889–7907, 2014.
- 521 Ban, N., Caillaud, C., Coppola, E., Pichelli, E., Sobolowski, S., Adinolfi, M., Ahrens, B., Alias, A., Anders, I., Bastin, S., et al.: The first  
522 multi-model ensemble of regional climate simulations at kilometer-scale resolution, part I: evaluation of precipitation, *Climate Dynamics*,  
523 57, 275–302, 2021.
- 524 Barlage, M., Chen, F., Rasmussen, R., Zhang, Z., and Miguez-Macho, G.: The importance of scale-dependent groundwater processes in  
525 land-atmosphere interactions over the central United States, *Geophysical Research Letters*, 48, e2020GL092171, 2021.
- 526 Brown, A., Dowdy, A., and Lane, T. P.: Convection-permitting climate model representation of severe convective wind gusts and future  
527 changes in southeastern Australia, *Natural Hazards and Earth System Sciences*, 24, 3225–3243, 2024.
- 528 Chu, H., Christianson, D. S., Cheah, Y.-W., Pastorello, G., O'Brien, F., Geden, J., Ngo, S.-T., Hollowgrass, R., Leibowitz, K., Beekwilder,  
529 N. F., et al.: AmeriFlux BASE data pipeline to support network growth and data sharing, *Scientific Data*, 10, 614, 2023.
- 530 Clark, P., Roberts, N., Lean, H., Ballard, S. P., and Charlton-Perez, C.: Convection-permitting models: A step-change in rainfall forecasting,  
531 *Meteorological Applications*, 23, 165–181, 2016.
- 532 Dee, D. P., Uppala, S., Simmons, A. J., Berrisford, P., Poli, P., Kobayashi, S., Andrae, U., Balmaseda, M., Balsamo, G., Bauer, d. P., et al.: The  
533 ERA-Interim reanalysis: Configuration and performance of the data assimilation system, *Quarterly Journal of the royal meteorological*  
534 *society*, 137, 553–597, <https://doi.org/https://doi.org/10.1002/qj.828>, 2011.
- 535 DeMott, C. A., Klingaman, N. P., and Woolnough, S. J.: Atmosphere-ocean coupled processes in the Madden-Julian oscillation, *Reviews of*  
536 *Geophysics*, 53, 1099–1154, 2015.
- 537 Deser, C., Phillips, A., Bourdette, V., and Teng, H.: Uncertainty in climate change projections: the role of internal variability, *Climate*  
538 *dynamics*, 38, 527–546, 2012.
- 539 Dipankar, A., Bianco, M., Bukenberger, M., Ehrenguber, T., Farabullini, N., Gopal, A., Hupp, D., Jocksch, A., Kellerhals, S., Kroll, C. A.,  
540 Lapillonne, X., Leclair, M., Luz, M., Müller, C., Ong, C. R., Osuna, C., Pothapakula, P., Röthlin, M., Sawyer, W., Serafini, G., Vogt, H.,  
541 Weber, B., and Schulthess, T.: Toward Exascale Climate Modelling: A Python DSL Approach to ICON's (Icosahedral Non-hydrostatic)  
542 Dynamical Core (icon-exclaim v0.2.0), *EGUsphere*, 2025, 1–26, <https://doi.org/10.5194/egusphere-2025-4808>, 2025.
- 543 Dominguez, F., Rasmussen, R., Liu, C., Ikeda, K., Prein, A., Varble, A., Arias, P. A., Bacmeister, J., Bettolli, M. L., Callaghan, P., et al.:  
544 Advancing South American water and climate science through multidecadal convection-permitting modeling, *Bulletin of the American*  
545 *Meteorological Society*, 105, E32–E44, 2024.



- 546 Donahue, A. S., Caldwell, P. M., Bertagna, L., Beydoun, H., Bogenschutz, P. A., Bradley, A., Clevenger, T. C., Foucar, J., Golaz, C., Guba,  
547 O., et al.: To exascale and beyond—The Simple Cloud-Resolving E3SM Atmosphere Model (SCREAM), a performance portable global  
548 atmosphere model for cloud-resolving scales, *Journal of Advances in Modeling Earth Systems*, 16, e2024MS004 314, 2024.
- 549 Donat, M. G., Lowry, A. L., Alexander, L. V., O’Gorman, P. A., and Maher, N.: More extreme precipitation in the world’s dry and wet  
550 regions, *Nature Climate Change*, 6, 508–513, 2016.
- 551 Dunn, Robert J. H.: HadISD.3.4.0: Product User Guide, Met Office Hadley Centre, Exeter, UK, <https://hadleyserver.metoffice.gov.uk/hadis>  
552 [d/hadis\\_v340\\_2023f\\_product\\_user\\_guide.pdf](https://hadleyserver.metoffice.gov.uk/hadis), version 3.4.0 (2023f) of the HadISD dataset, updated 12 Jan 2024., 2024.
- 553 Dunn, R. J., Willett, K. M., Parker, D. E., and Mitchell, L.: Expanding HadISD: Quality-controlled, sub-daily station data from 1931,  
554 *Geoscientific Instrumentation, Methods and Data Systems*, 5, 473–491, 2016.
- 555 Feng, Z., Prein, A. F., Kukulies, J., Fiolleau, T., Jones, W. K., Maybee, B., Moon, Z. L., Núñez Ocasio, K. M., Dong, W., Molina, M. J., et al.:  
556 Mesoscale convective systems tracking method intercomparison (MCSMIP): Application to DYAMOND global km-scale simulations,  
557 *Journal of Geophysical Research: Atmospheres*, 130, e2024JD042 204, 2025.
- 558 Gahtan, J., Knapp, K. R., Schreck, C. J. I., Diamond, H. J., Kossin, J. P., and Kruk, M. C.: International Best Track Archive for Climate  
559 Stewardship (IBTrACS) Project, Version 4.01, NOAA National Centers for Environmental Information, <https://doi.org/10.25921/82ty->  
560 [9e16](https://doi.org/10.25921/82ty-), 2024.
- 561 Gentry, M. S. and Lackmann, G. M.: Sensitivity of simulated tropical cyclone structure and intensity to horizontal resolution, *Monthly*  
562 *Weather Review*, 138, 688–704, 2010.
- 563 Giorgi, F. and Gutowski Jr, W. J.: Regional dynamical downscaling and the CORDEX initiative, *Annual review of environment and resources*,  
564 40, 467–490, 2015.
- 565 Giorgi, F., Jones, C., Asrar, G. R., et al.: Addressing climate information needs at the regional level: the CORDEX framework, *World*  
566 *Meteorological Organization (WMO) Bulletin*, 58, 175, 2009.
- 567 Grasselt, R., Schuttemeyer, D., Warrach-Sagi, K., Ament, F., and Simmer, C.: Validation of TERRA-ML with discharge measurements,  
568 *Meteorologische Zeitschrift*, 17, 763, 2008.
- 569 Gutmann, E. D., Rasmussen, R. M., Liu, C., Ikeda, K., Bruyere, C. L., Done, J. M., Garrè, L., Friis-Hansen, P., and Veldore, V.: Changes in  
570 hurricanes from a 13-yr convection-permitting pseudo-global warming simulation, *Journal of Climate*, 31, 3643–3657, 2018.
- 571 He, J., Hong, L., Shao, C., and Tang, W.: Global evaluation of simulated surface shortwave radiation in CMIP6 models, *Atmospheric*  
572 *Research*, 292, 106 896, 2023.
- 573 Hersbach, H., Bell, B., Berrisford, P., Hirahara, S., Horányi, A., Muñoz-Sabater, J., Nicolas, J., Peubey, C., Radu, R., Schepers, D., et al.:  
574 The ERA5 global reanalysis, *Quarterly journal of the royal meteorological society*, 146, 1999–2049, 2020.
- 575 Hohenegger, C., Brockhaus, P., Bretherton, C. S., and Schär, C.: The soil moisture–precipitation feedback in simulations with explicit and  
576 parameterized convection, *Journal of Climate*, 22, 5003–5020, 2009.
- 577 Huffman, G. J., Bolvin, D. T., Braithwaite, D., Hsu, K.-L., Joyce, R. J., Kidd, C., Nelkin, E. J., Sorooshian, S., Stocker, E. F., Tan, J.,  
578 et al.: Integrated multi-satellite retrievals for the global precipitation measurement (GPM) mission (IMERG), in: *Satellite precipitation*  
579 *measurement: Volume 1*, pp. 343–353, Springer, 2020.
- 580 Ikeda, K., Rasmussen, R., Liu, C., Newman, A., Chen, F., Barlage, M., Gutmann, E., Dudhia, J., Dai, A., Luce, C., et al.: Snowfall and  
581 snowpack in the Western US as captured by convection permitting climate simulations: Current climate and pseudo global warming future  
582 climate, *Climate Dynamics*, 57, 2191–2215, 2021.



- 583 IPCC: Climate Change 2023: Synthesis Report. Contribution of Working Groups I, II and III to the Sixth Assessment Report  
584 of the Intergovernmental Panel on Climate Change, Intergovernmental Panel on Climate Change (IPCC), Geneva, Switzerland,  
585 <https://doi.org/10.59327/IPCC/AR6-9789291691647>, 2023.
- 586 Janowiak, J., Joyce, B., and Xie, P.: NCEP/CPC L3 Half Hourly 4km global (60S–60N) Merged IR V1. Greenbelt, MD, Goddard Earth  
587 Sciences Data and Information Services Center (GES DISC), 2017.
- 588 Judt, F. and Rios-Berrios, R.: Resolved convection improves the representation of equatorial waves and tropical rainfall variability in a global  
589 nonhydrostatic model, *Geophysical Research Letters*, 48, e2021GL093265, 2021.
- 590 Judt, F., Klocke, D., Rios-Berrios, R., Vanniere, B., Ziemer, F., Auger, L., Biercamp, J., Bretherton, C., Chen, X., Düben, P., et al.: Tropical  
591 cyclones in global storm-resolving models, *Journal of the Meteorological Society of Japan. Ser. II*, 99, 579–602, 2021.
- 592 Jung, H. and Knippertz, P.: Link between the time-space behavior of rainfall and 3d dynamical structures of equatorial waves in global  
593 convection-permitting simulations, *Geophysical Research Letters*, 50, e2022GL100973, 2023.
- 594 Kendon, E., Prein, A. F., Senior, C., and Stirling, A.: Challenges and outlook for convection-permitting climate modelling, *Philosophical  
595 Transactions of the Royal Society A*, 379, 20190547, 2021.
- 596 Kendon, E. J., Ban, N., Roberts, N. M., Fowler, H. J., Roberts, M. J., Chan, S. C., Evans, J. P., Fosser, G., and Wilkinson, J. M.: Do convection-  
597 permitting regional climate models improve projections of future precipitation change?, *Bulletin of the American Meteorological Society*,  
598 98, 79–93, 2017.
- 599 Kiladis, G. N., Wheeler, M. C., Haertel, P. T., Straub, K. H., and Roundy, P. E.: Convectively coupled equatorial waves, *Reviews of Geo-  
600 physics*, 47, 2009.
- 601 Kinne, S.: The MACv2 aerosol climatology, *Tellus B: Chemical and Physical Meteorology*, 71, 1–21, 2019.
- 602 Knaff, J. A. and Zehr, R. M.: Reexamination of tropical cyclone wind–pressure relationships, *Weather and Forecasting*, 22, 71–88, 2007.
- 603 Knapp, K. R., Kruk, M. C., Levinson, D. H., Diamond, H. J., and Neumann, C. J.: The international best track archive for climate stewardship  
604 (IBTrACS) unifying tropical cyclone data, *Bulletin of the American Meteorological Society*, 91, 363–376, 2010.
- 605 Lange, S.: Bias correction of surface downwelling longwave and shortwave radiation for the EWEMBI dataset, *Earth System Dynamics*, 9,  
606 627–645, 2018.
- 607 Langendijk, G., Rechid, D., Sieck, K., and Jacob, D.: Added value of convection-permitting simulations for understanding future urban  
608 humidity extremes: case studies for Berlin and its surroundings, *Weather and Climate Extremes*, 33, 100367, 2021.
- 609 Liebmann, B. and Smith, C. A.: Description of a Complete (Interpolated) Outgoing Longwave Radiation Dataset, *Bulletin of the American  
610 Meteorological Society*, 77, 1275–1277, <http://www.jstor.org/stable/26233278>, 1996.
- 611 Liu, C., Ikeda, K., Rasmussen, R., Barlage, M., Newman, A. J., Prein, A. F., Chen, F., Chen, L., Clark, M., Dai, A., et al.: Continental-scale  
612 convection-permitting modeling of the current and future climate of North America, *Climate Dynamics*, 49, 71–95, 2017.
- 613 Lucas-Picher, P., Argüeso, D., Brisson, E., Trambly, Y., Berg, P., Lemonsu, A., Kotlarski, S., and Caillaud, C.: Convection-permitting  
614 modeling with regional climate models: Latest developments and next steps, *Wiley Interdisciplinary Reviews: Climate Change*, 12, e731,  
615 2021.
- 616 Lucas-Picher, P., Brisson, E., Caillaud, C., Alias, A., Nabat, P., Lemonsu, A., Poncet, N., Cortés Hernandez, V. E., Michau, Y., Doury, A.,  
617 et al.: Evaluation of the convection-permitting regional climate model CNRM-AROME41t1 over Northwestern Europe, *Climate Dynam-  
618 ics*, 62, 4587–4615, 2024.
- 619 Mapes, B., Tulich, S., Lin, J., and Zuidema, P.: The mesoscale convection life cycle: Building block or prototype for large-scale tropical  
620 waves?, *Dynamics of atmospheres and oceans*, 42, 3–29, 2006.



- 621 Merchant, C. J., Embury, O., Bulgin, C. E., Block, T., Corlett, G. K., Fiedler, E., Good, S. A., Mittaz, J., Rayner, N. A., Berry, D., et al.:  
622 Satellite-based time-series of sea-surface temperature since 1981 for climate applications, *Scientific data*, 6, 223, 2019.
- 623 Paredes, E. G., Groner, L., Ubbiali, S., Vogt, H., Madonna, A., Mariotti, K., Cruz, F., Benedicic, L., Bianco, M., VandeVondele, J., et al.:  
624 Gt4py: High performance stencils for weather and climate applications using python, *arXiv preprint arXiv:2311.08322*, 2023.
- 625 Pastorello, G., Trotta, C., Canfora, E., Chu, H., Christianson, D., Cheah, Y.-W., Poindexter, C., Chen, J., Elbashandy, A., Humphrey, M.,  
626 et al.: The FLUXNET2015 dataset and the ONEFlux processing pipeline for eddy covariance data, *Scientific data*, 7, 225, 2020.
- 627 Perkins-Kirkpatrick, S. and Lewis, S.: Increasing trends in regional heatwaves, *Nature communications*, 11, 3357, 2020.
- 628 Pichelli, E., Coppola, E., Sobolowski, S., Ban, N., Giorgi, F., Stocchi, P., Alias, A., Belušić, D., Berthou, S., Caillaud, C., et al.: The first multi-  
629 model ensemble of regional climate simulations at kilometer-scale resolution part 2: historical and future simulations of precipitation,  
630 *Climate Dynamics*, 56, 3581–3602, 2021.
- 631 Prein, A.: andreas-prein/icon2.5\_dyamond3\_paper: vo.1.0.0, <https://doi.org/10.5281/zenodo.18007290>, 2025.
- 632 Prein, A. F.: Thunderstorm straight line winds intensify with climate change, *Nature Climate Change*, 13, 1353–1359, 2023.
- 633 Prein, A. F. and Gobiet, A.: Impacts of uncertainties in European gridded precipitation observations on regional climate analysis, *International*  
634 *Journal of Climatology*, 37, 305–327, 2017.
- 635 Prein, A. F., Gobiet, A., Suklitsch, M., Truhetz, H., Awan, N. K., Keuler, K., and Georgievski, G.: Added value of convection permitting  
636 seasonal simulations, *Climate Dynamics*, 41, 2655–2677, 2013.
- 637 Prein, A. F., Langhans, W., Fosser, G., Ferrone, A., Ban, N., Goergen, K., Keller, M., Tölle, M., Gutjahr, O., Feser, F., et al.: A review on  
638 regional convection-permitting climate modeling: Demonstrations, prospects, and challenges, *Reviews of geophysics*, 53, 323–361, 2015.
- 639 Prein, A. F., Rasmussen, R. M., Ikeda, K., Liu, C., Clark, M. P., and Holland, G. J.: The future intensification of hourly precipitation extremes,  
640 *Nature climate change*, 7, 48–52, 2017.
- 641 Prein, A. F., Liu, C., Ikeda, K., Bullock, R., Rasmussen, R. M., Holland, G. J., and Clark, M.: Simulating North American mesoscale  
642 convective systems with a convection-permitting climate model, *Climate Dynamics*, 55, 95–110, 2020.
- 643 Prein, A. F., Rasmussen, R., Wang, D., and Giangrande, S.: Sensitivity of organized convective storms to model grid spacing in current and  
644 future climates, *Philosophical Transactions of the Royal Society A*, 379, 20190 546, 2021.
- 645 Prein, A. F., Ge, M., Valle, A. R., Wang, D., and Giangrande, S. E.: Towards a unified setup to simulate mid-latitude and tropical mesoscale  
646 convective systems at kilometer-scales, *Earth and Space Science*, 9, e2022EA002 295, 2022.
- 647 Prein, A. F., Ban, N., Ou, T., Tang, J., Sakaguchi, K., Collier, E., Jayanarayanan, S., Li, L., Sobolowski, S., Chen, X., et al.: Towards  
648 ensemble-based kilometer-scale climate simulations over the third pole region, *Climate Dynamics*, 60, 4055–4081, 2023a.
- 649 Prein, A. F., Mooney, P. A., and Done, J. M.: The multi-scale interactions of atmospheric phenomenon in mean and extreme precipitation,  
650 *Earth's Future*, 11, e2023EF003 534, 2023b.
- 651 Prein, A. F., Feng, Z., Fiolleau, T., Moon, Z. L., Núñez Ocasio, K. M., Kukulies, J., Roca, R., Varble, A. C., Rehbein, A., Liu, C., et al.:  
652 Km-scale simulations of mesoscale convective systems over South America—A feature tracker intercomparison, *Journal of Geophysical*  
653 *Research: Atmospheres*, 129, e2023JD040 254, 2024.
- 654 Randall, D. A. and Emanuel, K.: The weather–climate schism, *Bulletin of the American Meteorological Society*, 105, E300–E305, 2024.
- 655 Raschendorfer, M., Simmer, C., and Gross, P.: Parameterisation of turbulent transport in the atmosphere, in: *Dynamics of multiscale earth*  
656 *systems*, pp. 167–185, Springer, 2003.



- 657 Roberts, M. J., Camp, J., Seddon, J., Vidale, P. L., Hodges, K., Vanniere, B., Mecking, J., Haarsma, R., Bellucci, A., Scoccimarro, E.,  
658 et al.: Impact of model resolution on tropical cyclone simulation using the HighResMIP-PRIMAVERA multimodel ensemble, *Journal of*  
659 *Climate*, 33, 2557–2583, 2020.
- 660 Sakradzija, M., Senf, F., Scheck, L., Ahlgrimm, M., and Klocke, D.: Local impact of stochastic shallow convection on clouds and precipitation  
661 in the tropical Atlantic, *Monthly Weather Review*, 148, 5041–5062, 2020.
- 662 Savre, J. and Craig, G.: Fitting cumulus cloud size distributions from idealized cloud resolving model simulations, *Journal of Advances in*  
663 *Modeling Earth Systems*, 15, e2022MS003 360, 2023.
- 664 Schär, C., Leuenberger, D., Fuhrer, O., Lüthi, D., and Girard, C.: A new terrain-following vertical coordinate formulation for atmospheric  
665 prediction models, *Monthly Weather Review*, 130, 2459–2480, 2002.
- 666 Schär, C., Fuhrer, O., Arteaga, A., Ban, N., Charpielloz, C., Di Girolamo, S., Hentgen, L., Hoefler, T., Lapillonne, X., Leutwyler, D., et al.:  
667 Kilometer-scale climate models: Prospects and challenges, *Bulletin of the American Meteorological Society*, 101, E567–E587, 2020.
- 668 Schellekens, J., Dutra, E., Martínez-de La Torre, A., Balsamo, G., Van Dijk, A., Sperna Weiland, F., Minvielle, M., Calvet, J.-C., Decharme,  
669 B., Eisner, S., et al.: A global water resources ensemble of hydrological models: the earthH2Observe Tier-1 dataset, *Earth System Science*  
670 *Data*, 9, 389–413, <https://doi.org/10.5194/essd-9-389-2017>, 2017.
- 671 Schenkel, B. A. and Hart, R. E.: An examination of tropical cyclone position, intensity, and intensity life cycle within atmospheric reanalysis  
672 datasets, *Journal of Climate*, 25, 3453–3475, 2012.
- 673 Schmidli, J., Böing, S., and Fuhrer, O.: Accuracy of simulated diurnal valley winds in the Swiss Alps: Influence of grid resolution, topography  
674 filtering, and land surface datasets, *Atmosphere*, 9, 196, 2018.
- 675 Schrodin, R. and Heise, E.: The multi-layer version of the DWD soil model TERRA\_LM, DWD Offenbach, Germany, 2001.
- 676 Schulz, J.-P. and Vogel, G.: Improving the processes in the land surface scheme TERRA: Bare soil evaporation and skin temperature,  
677 *Atmosphere*, 11, 513, 2020.
- 678 Segura, H., Bayley, C., Fievét, R., Glöckner, H., Günther, M., Klufft, L., Naumann, A., Ortega, S., Praturi, D., Rixen, M., et al.: A single  
679 tropical rainbelt in global storm-resolving models: The role of surface heat fluxes over the warm pool, *Journal of Advances in Modeling*  
680 *Earth Systems*, 17, e2024MS004 897, 2025a.
- 681 Segura, H., Pedruzo-Bagazgoitia, X., Weiss, P., Müller, S. K., Rackow, T., Lee, J., Dolores-Tesillos, E., Benedict, I., Aengenheyster, M.,  
682 Aguridan, R., et al.: nextGEMS: entering the era of kilometer-scale Earth system modeling, *EGUsphere*, 2025, 1–39, 2025b.
- 683 Seifert, A.: A revised cloud microphysical parameterization for COSMO-LME, *COSMO Newsletter 7*, Consortium for Small-Scale Mod-  
684 elling, <http://www.cosmo-model.org>, proceedings from the 8th COSMO General Meeting, Bucharest, 2006, 2008.
- 685 Seneviratne, S. I., Zhang, X., Adnan, M., Badi, W., Dereczynski, C., Luca, A. D., Ghosh, S., Iskandar, I., Kossin, J., Lewis, S., et al.: Weather  
686 and climate extreme events in a changing climate, 2021.
- 687 Soares, P. M., Careto, J. A., Cardoso, R. M., Goergen, K., Katragkou, E., Sobolowski, S., Coppola, E., Ban, N., Belušić, D., Berthou, S., et al.:  
688 The added value of km-scale simulations to describe temperature over complex orography: the CORDEX FPS-Convection multi-model  
689 ensemble runs over the Alps, *Climate Dynamics*, 62, 4491–4514, 2024.
- 690 Song, Y., Broxton, P. D., Ehsani, M. R., and Behrang, A.: Assessment of snowfall accumulation from satellite and reanalysis products using  
691 SNOTEL observations in Alaska, *Remote Sensing*, 13, 2922, 2021.
- 692 Stevens, B., Satoh, M., Auger, L., Biercamp, J., Bretherton, C. S., Chen, X., Düben, P., Judt, F., Khairoutdinov, M., Klocke, D., et al.: DYA-  
693 MOND: the DYNAMICS of the Atmospheric general circulation Modeled On Non-hydrostatic Domains, *Progress in Earth and Planetary*  
694 *Science*, 6, 1–17, 2019.



- 695 Takasuka, D., Satoh, M., Miyakawa, T., Kodama, C., Klocke, D., Stevens, B., Vidale, P. L., and Terai, C. R.: A protocol and analysis of  
696 year-long simulations of global storm-resolving models and beyond, *Progress in Earth and Planetary Science*, 11, 66, 2024.
- 697 Taylor, M., Caldwell, P. M., Bertagna, L., Clevenger, C., Donahue, A., Foucar, J., Guba, O., Hillman, B., Keen, N., Krishna, J., et al.: The  
698 simple cloud-resolving E3SM atmosphere model running on the Frontier exascale system, in: *Proceedings of the international conference  
699 for high performance computing, networking, storage and analysis*, pp. 1–11, 2023.
- 700 Trenberth, K. E.: 24.5-Year Surface Radiation Budget Data Set Released, 2011.
- 701 Virtanen, P., Gommers, R., Oliphant, T. E., Haberland, M., Reddy, T., Cournapeau, D., Burovski, E., Peterson, P., Weckesser, W., Bright, J.,  
702 et al.: SciPy 1.0: fundamental algorithms for scientific computing in Python, *Nature methods*, 17, 261–272, 2020.
- 703 Weber, N. J. and Mass, C. F.: Subseasonal weather prediction in a global convection-permitting model, *Bulletin of the American Meteorolo-  
704 gical Society*, 100, 1079–1089, 2019.
- 705 Weedon, G. P., Balsamo, G., Bellouin, N., Gomes, S., Best, M. J., and Viterbo, P.: The WFDEI meteorological forcing data  
706 set: WATCH Forcing Data methodology applied to ERA-Interim reanalysis data, *Water Resources Research*, 50, 7505–7514,  
707 <https://doi.org/https://doi.org/10.1002/2014WR015638>, 2014.
- 708 Wheeler, M. and Kiladis, G. N.: Convectively Coupled Equatorial Waves: Analysis of Clouds and Temperature in the  
709 Wavenumber–Frequency Domain, *Journal of the Atmospheric Sciences*, 56, 374 – 399, [https://doi.org/10.1175/1520-  
710 0469\(1999\)056<0374:CCEWAO>2.0.CO;2](https://doi.org/10.1175/1520-0469(1999)056<0374:CCEWAO>2.0.CO;2), 1999.
- 711 World Climate Research Programme: Report of the WCRP km-scale modeling workshop, 3–7 October 2022, hybrid format, Tech. Rep.  
712 08/2022, World Climate Research Programme (WCRP), Geneva, Switzerland, [https://www.wcrp-climate.org/WCRP-publications/2022  
713 /WCRP\\_Report\\_08-2022\\_k-scale-report-final.pdf](https://www.wcrp-climate.org/WCRP-publications/2022/WCRP_Report_08-2022_k-scale-report-final.pdf), 2022.
- 714 Yu, H., Prein, A. F., Qi, D., and Wang, K.: Mesoscale convective systems in Northeast China from satellite products, global reanalysis, and  
715 kilometer-scale modeling, *Geophysical Research Letters*, 52, e2024GL112 349, 2025.
- 716 Zängl, G., Reinert, D., Rípodas, P., and Baldauf, M.: The ICON (ICOsahedral Non-hydrostatic) modelling framework of DWD and MPI-M:  
717 Description of the non-hydrostatic dynamical core, *Quarterly Journal of the Royal Meteorological Society*, 141, 563–579, 2015.
- 718 Zhang, Z., Varble, A. C., Feng, Z., Marquis, J. N., Hardin, J. C., and Zipser, E. J.: Dependencies of simulated convective cell and system  
719 growth biases on atmospheric instability and model resolution, *Journal of Geophysical Research: Atmospheres*, 129, e2024JD041 090,  
720 2024.

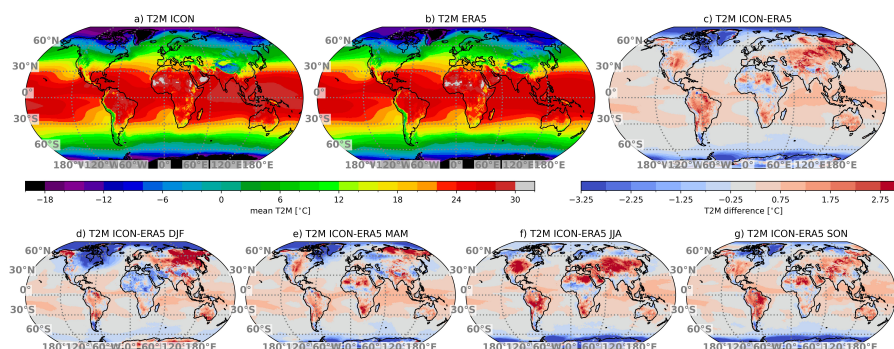


**Figure 1.** Annual mean daily T2M in ICON (a), ERA5 (b), and their difference (c) during the simulation period. Seasonal average T2M differences are shown in (d–g).

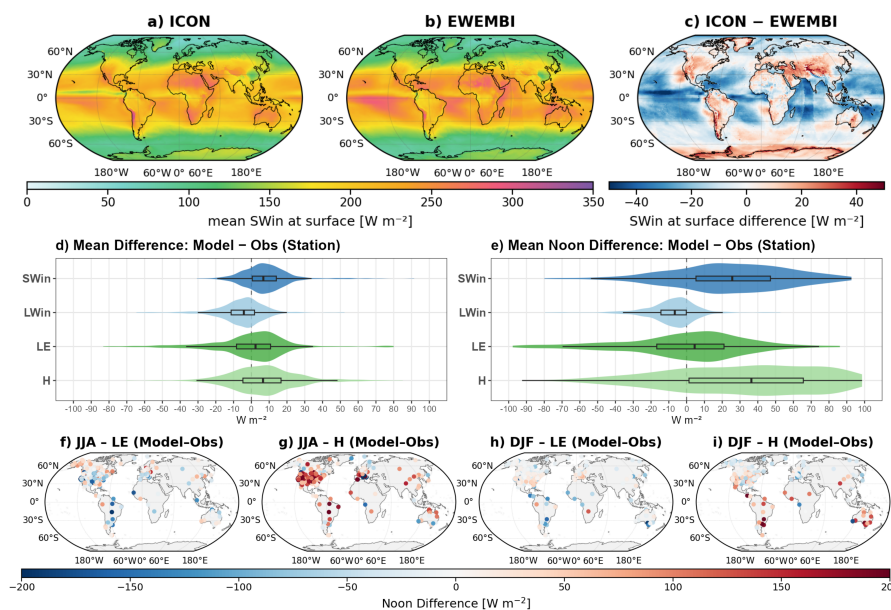


**Figure 2.** (a–c) Daily mean incoming shortwave radiation at the surface (SWin) from (a) ICON (2020–2024), (b) the EWEMBI (2012–2016) observational dataset, and (c) their difference (ICON - EWEMBI). (d–e) Violin plots of station-based differences (model - observations) for mean (d) and mean local solar time noon (e) surface fluxes: SWin, incoming longwave radiation (LWin), latent heat flux (LE), and sensible heat flux (H). Boxes indicate the interquartile range and median difference. (f–i) Station-based mean noon differences (model - observations) for LE and H during JJA (June, July, August) and DJF (December, January, February).

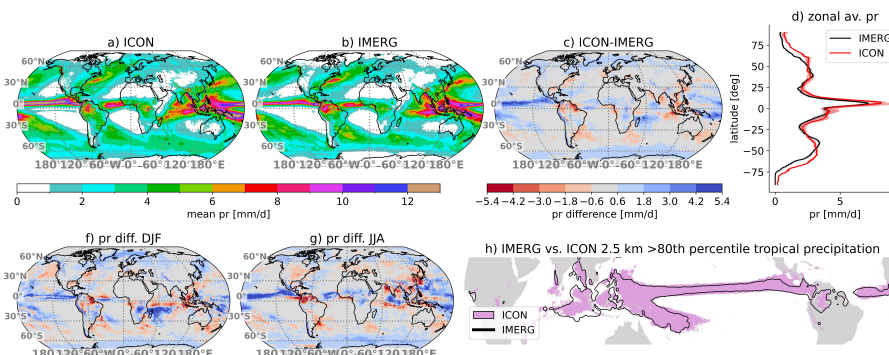


**Figure 3.** Annual mean daily precipitation in ICON (a), IMERG (b), and their difference (c) during the simulation period. DJF and JJA average precipitation differences are shown in (f) and (g), respectively. Mean zonal average precipitation is shown in (d) with inter-annual spread shown in contours. The area that covers the 80th percentile of tropical average precipitation ( $\pm 20^\circ$ ) from ICON (purple) and IMERG (black contour) is shown in (h).

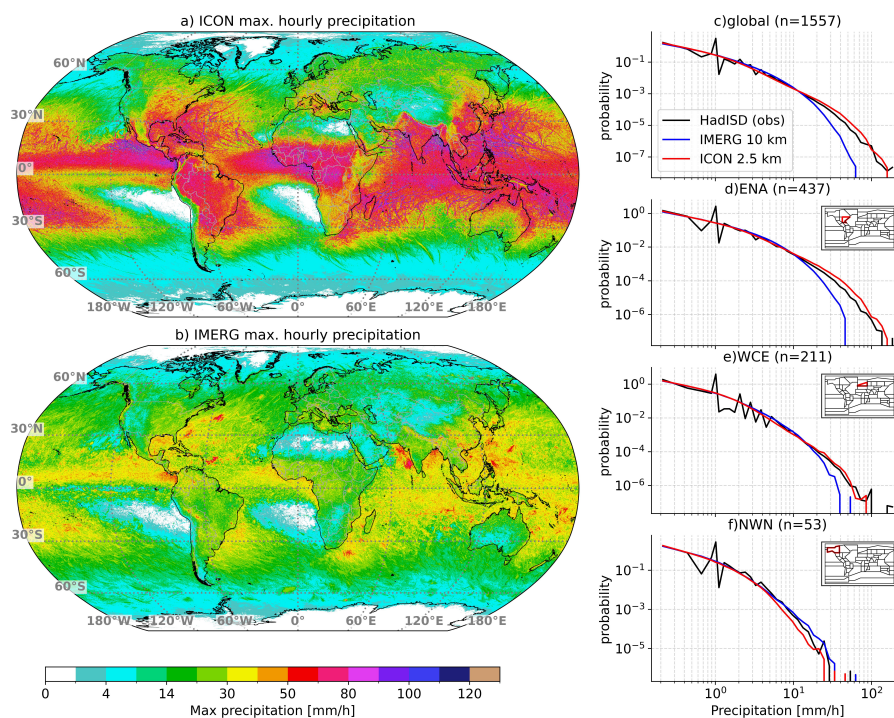


**Figure 4.** Hourly maximum precipitation accumulation during the simulation period from ICON (a) and IMERG (b) on the  $0.1^\circ$  IMERG grid. Probability density functions for hourly precipitation comparing ICON (red) and IMERG (blue) against HadISD station observations (black) globally (c) and in the Eastern North America (ENA, d), Western Central Europe (WCE, e), and North Western North America (NWN, f) region. The locations of these regions are shown in the inset maps in (b–f). The underlying station density in the HadISD dataset is shown in Fig. S1.

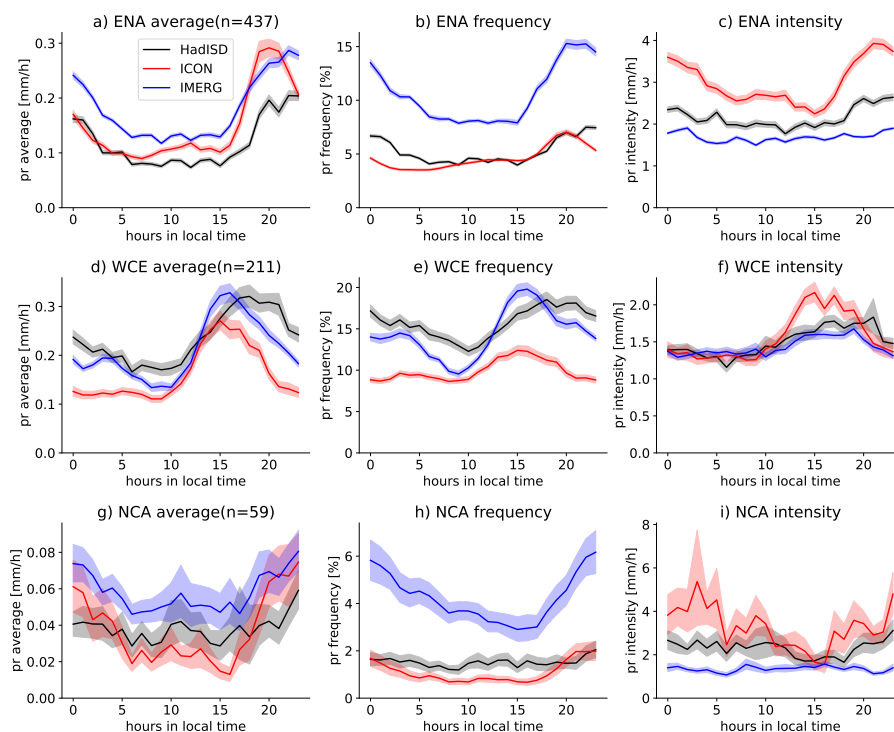


**Figure 5.** Hourly precipitation diurnal cycle during June, July, and August of average precipitation (a, d, g), precipitation frequency (b,e,h), and precipitation intensity (c,f,i). Results are shown for the Eastern North America (a–c), Western Central Europe (WCE), and North Central America (NCA) region. Precipitation frequency and intensity statistics are based on a precipitation threshold of  $\geq 0.1 \text{ mm h}^{-1}$ . Data is based on HadISD records (black lines) that have more than 50 % coverage. Missing values in HadISD are also removed in the ICON (red lines) and IMERG (blue lines) data. Contours show station sampling uncertainties based on the 10 to 90 percentile value of 10,000 bootstrap samples (with replacement).

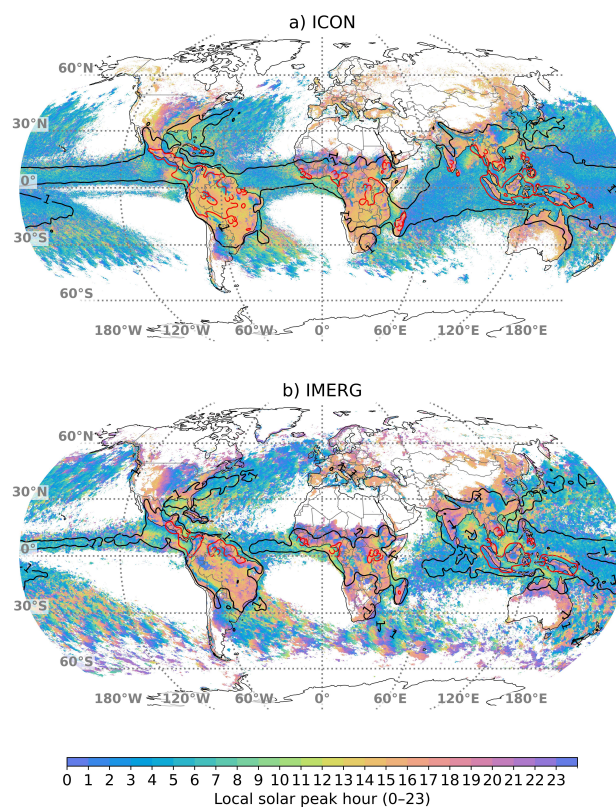


**Figure 6.** Color-coded local peak time of precipitation diurnal cycle in ICON (a) and IMERG (b). Colored regions show areas where the precipitation diurnal cycle amplitude is larger than 40 % of the mean precipitation. Black/red contours show regions where the amplitude is larger than 100 %/200 % of the mean precipitation. Data from all months is used in the tropics ( $\leq \pm 30^\circ$ ), data from June, July, and August is used for latitudes  $> 30^\circ$ , and data from December, January, and February is used for latitudes  $< -30^\circ$ .

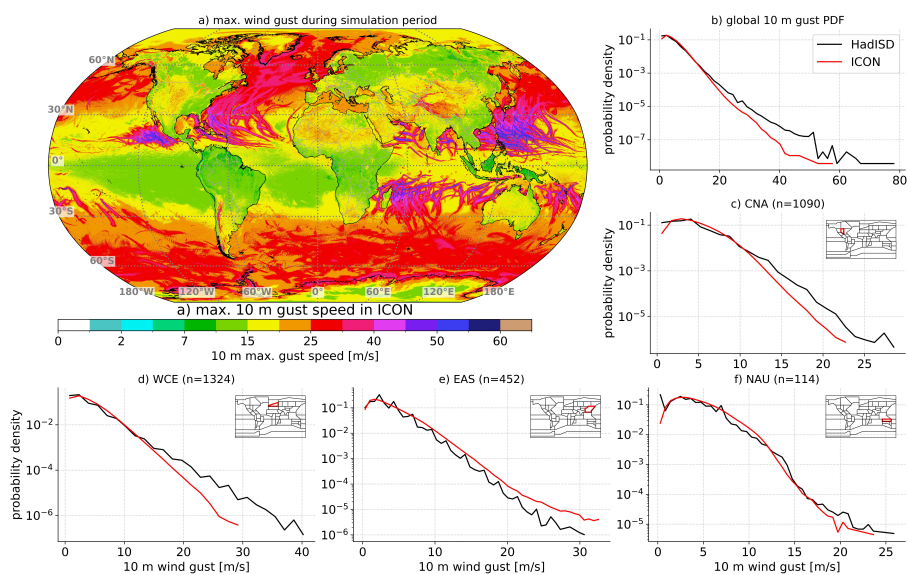


**Figure 7.** Maximum instantaneous simulated 10 m above surface wind from hourly model output during the simulation period (a). Probability density functions for hourly sampled winds from HadISD (black line) and ICON (red line). Statistics are shown for all stations globally (b; see Fig. S3 for station locations) and for the Central North America (CNA; c), Western Central Europe (WCE; d), East Asia (EAS; e), and North Australia (NAU; f) region. The number of stations (n) in each region is shown in the panel titles.

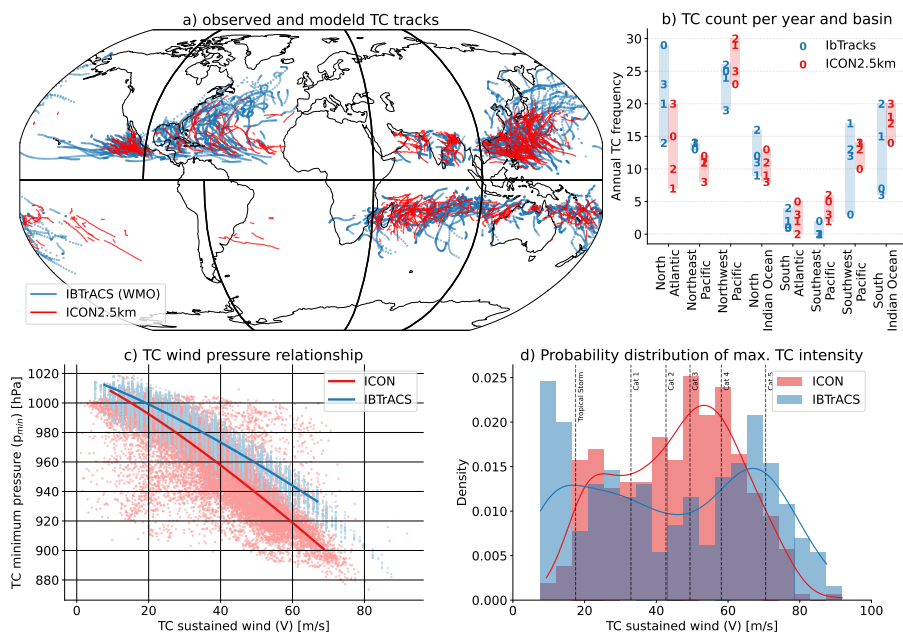


**Figure 8.** Tropical cyclone (TC) tracks from IBTrACS (blue) and ICON (red) during the simulation period (a). Basin annual frequency of tropical cyclones (b) in 2020 (0; only April to December), 2021 (1), 2022 (2), and 2023 (3). Tropical cyclone pressure wind relationship (c) from IBTrACS (blue) and ICON (red). Thick lines show the fitted figure of  $V(p_{min}) = a(p_{ref} - p_{min})^b$  with  $p_{min}$  being the minimum cyclone pressure,  $V$  being the sustained wind speed, and  $p_{ref}$  being the reference pressure at zero wind speed. Probability density of lifetime peak tropical cyclone sustained wind speed in IBTrACS and ICON (d).

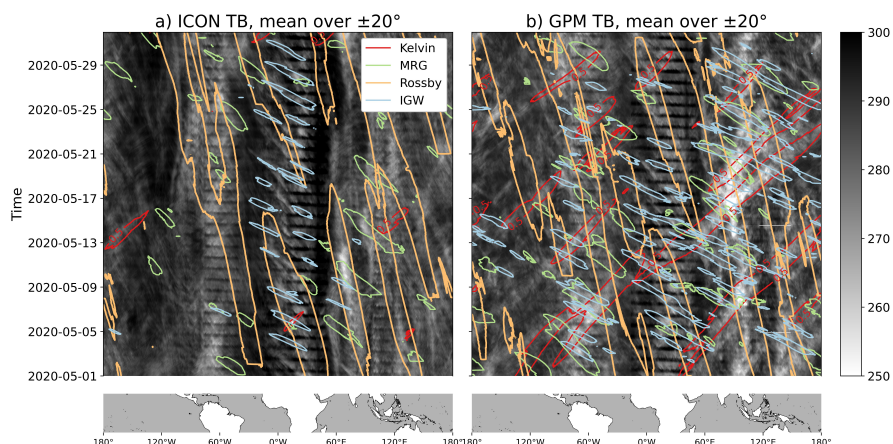


**Figure 9.** Hoffmüller diagrams of tropical average ( $\pm 20^\circ$ ) brightness temperature from ICON (a) and GPM-MERGIR (b) shown in gray contours for May 2020. Contours lines show Kelvin (red), Mixed Rossby Gravity (MRG, green), Rossby (orange), and Inertia Gravity (IGW, blue) waves.

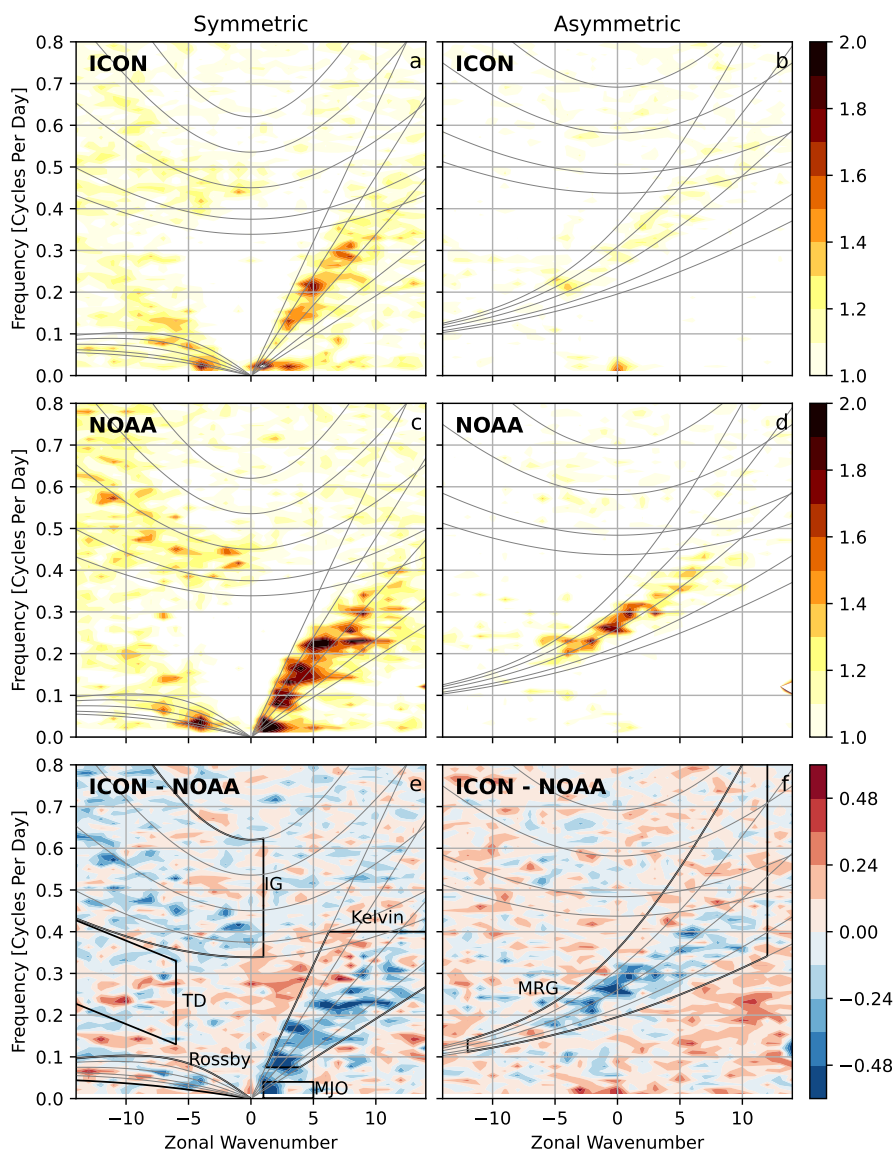


**Figure 10.** Wavenumber–frequency spectra of outgoing longwave radiation (OLR), divided by the background spectrum, from the ICON simulation (a, b) and NOAA satellite observations (c, d), along with their differences (e, f). Spectra are separated into symmetric (a, c, e) and antisymmetric (b, d, f) components. Gray curves indicate theoretical dispersion relations, while bold black outlines denote spectral windows associated with different equatorial wave modes: IG (inertia–gravity waves), TD (tropical depressions), Rossby, MJO (Madden–Julian Oscillation), Kelvin, and MRG (mixed Rossby–gravity waves).

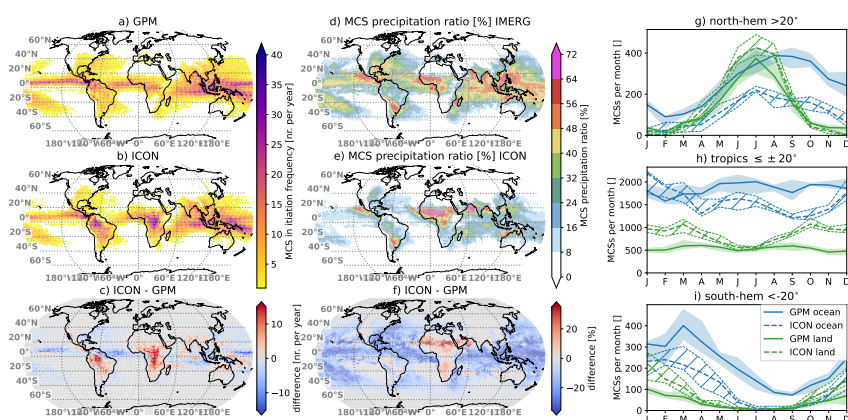


**Figure 11.** Annual average initiation frequency of MCSs in GPM (a), ICON (b), and their difference. Ratio of MCS precipitation compared to total precipitation averaged over the simulation period from GPM (d), ICON (e), and their difference (f). Monthly mean MCS frequency over land (green) and ocean (blue) in the northern hemisphere (g;  $>20^\circ$ ), the tropics (h;  $\leq \pm 20^\circ$ ), and the southern hemisphere (i;  $<20^\circ$ ). GPM results are shown with solid lines, while dashed lines show results based on ICON. The thick line is the median frequency, while the contours show the maximum and minimum spread over the four years.

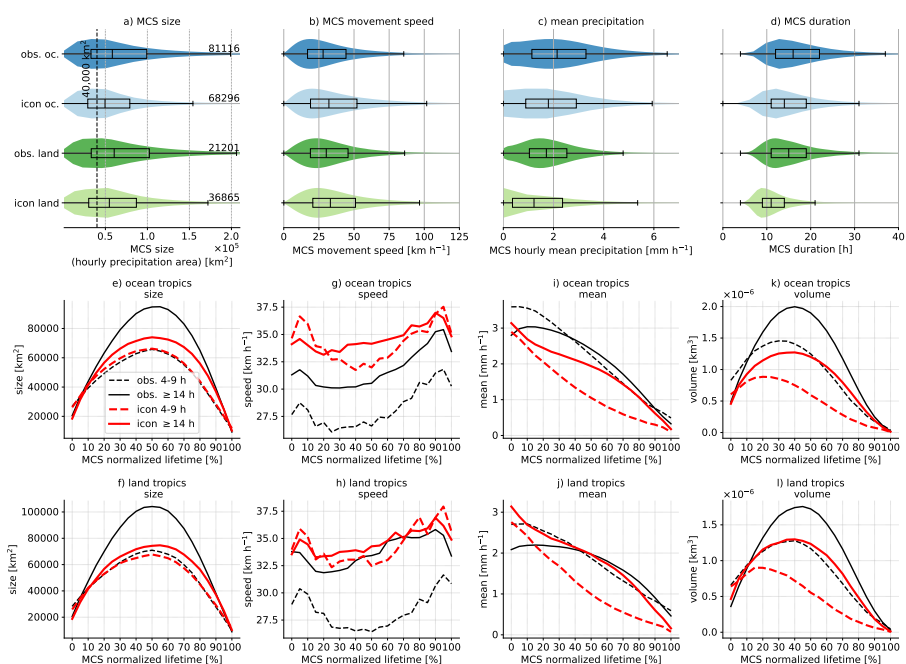


**Figure 12.** Violin and box-whisker plots for the distribution of tropical MCS sizes (a), speed (b), mean precipitation (c), and duration (d). The numbers right to the violins in (a) show the number of MCSs in each distribution. The lower panels show the normalized median evolution of short-lived (4-9 hours; dashed) and long-lived ( $\geq 14$  hours; solid) MCSs in GPM observations (black lines) and in ICON (red lines). The middle panels show results for tropical oceans while the lower panel shows tropical land regions.

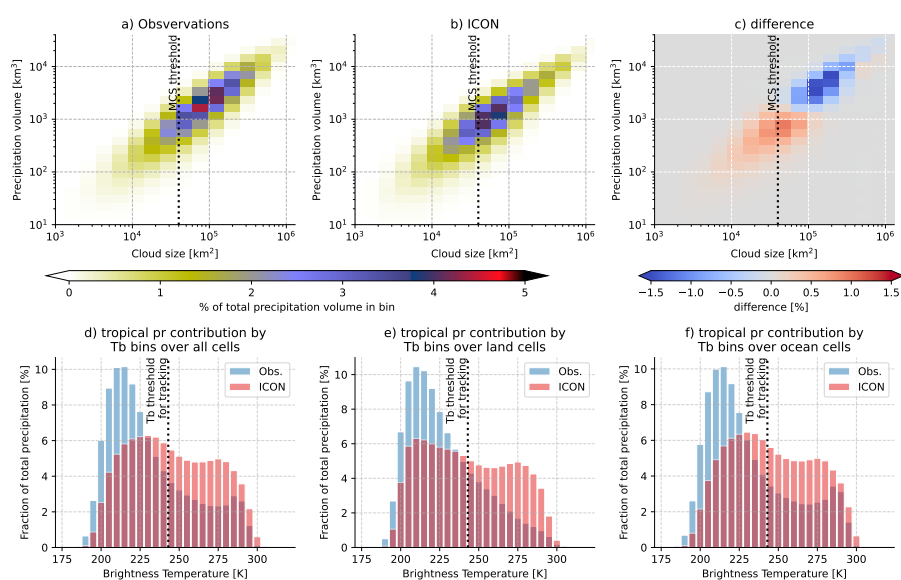


**Figure 13.** Relative contribution of tropical (latitude  $< \pm 20^\circ$ ) total precipitation from storms with cold cloud shields (Tb < 243 K) as a function of cloud shield size and precipitation volume under the cloud from observations (a), ICON (b), and their difference (c). The vertical dashed line shows the cloud shield threshold used for MCS classification. The fraction of total precipitation conditioned on Tb over the tropics (d), tropical land (e), and tropical ocean (f). The vertical dashed line shows the Tb threshold used for cold cloud identification.

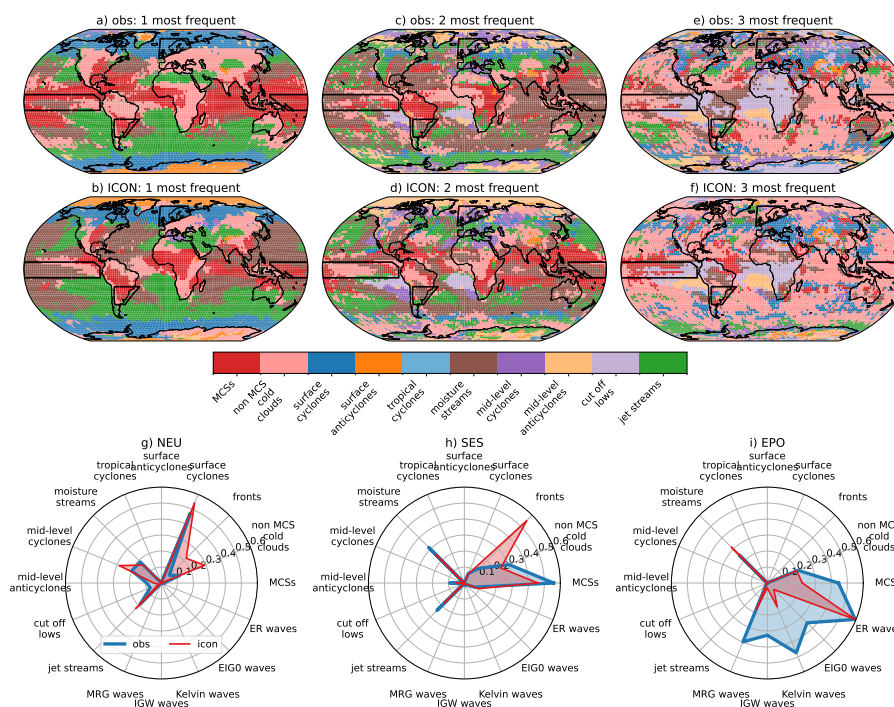


**Figure 14.** The most frequent (a,b), second most frequent (c,d), and third most frequent (e,f) atmospheric phenomena identified by the MOAAP algorithm that is co-located during the top 20 hourly precipitation events in the evaluation period. Observed/ICON results are shown in the top/middle panel. The data was up-scaled to a  $2.5^\circ$  grid to lower the signal-to-noise ratio. The same data is shown in panel (g–i) as the fractional frequency of the phenomenon in the Northern European (NEU), Southeast South America (SES), and Equatorial Pacific Ocean (EPO) regions (these regions are highlighted in the maps in (a–f)). A value of 0.5 means that 50% of all grid cells in a region had the corresponding phenomena co-located during a heavy precipitation event.